Advances in Geo-Energy Research

Vol. 22, No. 2, p. 134-153, 2026

Invited review

Nanoscale geomechanics and geochemistry of shale: Advances in atomic force microscopy applications for hydrocarbon recovery and carbon storage

Yujia Wang[1,2], Kouqi Liu[1,2]*, Hong Zhang[1,2], Yamin Wang[1,2], Danis Nurgaliev[3], Ameen Ahmed Al-Muntaser[3]

[1]*Institute of Energy, Peking University, Beijing 100871, P. R. China*

[2]*State Key Laboratory of Shale Oil and Gas Enrichment Mechanisms and Effective Development, Beijing 100083, P. R. China*

[3]*Department of Petroleum Engineering, Kazan Federal University, Kazan 420008, Russia*

Keywords:
Atomic force microscopy-based infrared spectroscopy
nanoindentation
unconventional shale reservoirs
nanoscale geomechanics

Cited as:
Wang, Y., Liu, K., Zhang, H., Wang, Y., Nurgaliev, D., Al-Muntaser, A. A. Nanoscale geomechanics and geochemistry of shale: Advances in atomic force microscopy applications for hydrocarbon recovery and carbon storage. Advances in Geo-Energy Research, 2026, 22(2): 134-153.
https://doi.org/10.46690/ager.2026.11.04

Abstract:
Shale reservoirs, as the cornerstone of global unconventional oil and gas production, are gradually becoming critical geological targets for carbon capture, utilization and storage. However, the complex multi-scale heterogeneity of these formations render traditional macroscopic geomechanical assessments insufficient. To characterize the nanomechanical, topographical and geochemical properties of organic-rich shales, this review synthesizes recent advancements in atomic force microscopy and specialized modes, such as PeakForce quantitative nanomechanical mapping and atomic force microscopy-based infrared spectroscopy. After examining the distinct mechanical responses of inorganic minerals versus organic macerals, a compliant organic framework is identified that influences bulk rock deformation. A key focus is placed on the geochemical evolution of organic matter, for which a maturity-dependent S-shaped evolutionary trend in Young's modulus associated with the transition from aliphatic-rich to aromatic-condensed structures is suggested. Furthermore, nanoscale fluid-solid interactions are discussed, and the role of surface potential heterogeneity and hydrated cation bridges in controlling wettability and adhesion is specifically considered. Finally, a pathway is outlined for integrating nanoscale atomic force microscopy data with artificial-intelligence analysis and multiscale modeling. The applicability boundaries between established nanoscale observations and forward-looking reservoir-scale propositions are also critically assessed. These advances could support sweet-spot identification, hydraulic-fracturing design and carbon-storage assessment, while engineering applications require further validation at the reservoir scale.

1. Introduction

Shale reservoirs have revolutionized the global energy landscape by transitioning from simple source rocks to critical unconventional targets, acting as self-generating and self-storing oil accumulations (Yang et al., 2017; Hu et al., 2021a). These fine-grained formations constitute 20%-50% of total global petroleum reserves, of which technically recoverable global reserves are estimated at 4.69×10^{10} tons (Bentley, 2002; Zou et al., 2019; Xu et al., 2022). Shales are also promising targets for carbon capture, utilization and storage because they adsorb carbon dioxide (CO_2) more strongly than methane (Mastalerz et al., 2012), and their nanoscale pore networks and low permeability further support long-

Yandy Scientific Press

*Corresponding author.
E-mail address: yujia.w@stu.pku.edu.cn (Yujia Wang); Kouqi.liu@pku.edu.cn (K. Liu); 2501110675@stu.pku.edu.cn (H. Zhang); yamin.wang@pku.edu.cn (Yamin Wang); Danis.Nourgaliev@kpfu.ru (D. Nurgaliev); aalmuntaser@mail.ru (A. A. Al-Muntaser).
2207-9963 © The Author(s) 2026.
Received September 8, 2026; revised October 7, 2026; accepted October 19, 2026; available online October 22, 2026.

term carbon sequestration while providing opportunities for enhanced oil recovery (Han et al., 2024).

Solid organic matter within shale is characterized as a highly heterogeneous geomacromolecule consisting of an intricate mixture of primary and secondary components (Hutton et al., 1994; Mastalerz et al., 2018). The primary fraction is identified as kerogen (insoluble in organic solvents) that is composed of various macerals (alginite, vitrinite and amorphinite) with unique biogenic origin and chemical reactivity (Hutton et al., 1994; Tyson, 1995; Mastalerz et al., 2012). The structural reorganization of these macerals occurs with increasing burial depth and thermal maturation. This process typically involves a shift from aliphatic-rich chains to graphite-like condensed aromatic structures (Bernard et al., 2012; Yang et al., 2017; Khatibi et al., 2018) and results in the formation of solid bitumen (a secondary maceral), which fills intergranular voids and develops secondary nanopores. The latter act as the dominant storage spaces in highly mature gas reservoirs (Curiale, 1986; Hutton et al., 1994). Bedding-parallel slip can further reorganize organic nanostructures while reducing organic micropore and mesopore volumes in highly deformed shales (Zhu et al., 2025).

Standard geomechanical assessments (triaxial and uniaxial compression tests) are insufficient for shales because they only provide average properties and do not consider the extreme heterogeneity of the nanocomposite rock fabric (Ulm and Abousleiman, 2006; Eliyahu et al., 2015). Traditional macroscopic testing is also expensive and destructive, requires large, well-preserved cores and cannot resolve nanometer-scale variations within the representative elementary volume (Bobko and Ulm, 2008; Bennett et al., 2015; Eliyahu et al., 2015). Furthermore, organic matter is significantly softer than the surrounding mineral matrix, with an elastic modulus of approximately 10 GPa compared with 70 GPa for quartz. Consequently, fracture propagation and wellbore stability are strongly influenced by organic matter (Zeszotarski et al., 2004; Yang et al., 2017). Macroscopic tools also fail to capture subtle phenomena like pop-in events that indicate the initiation of cracks at micro-scale pores beneath a certain stress point (Abedi et al., 2016; Liu and Ostadhassan, 2017; Liu et al., 2018a).

Atomic force microscopy (AFM) has emerged as a non-destructive tool that overcomes the diffraction limits of traditional microscopy, providing spatial resolutions of 5-10 nm (Javadpour et al., 2012; Dazzi and Prater, 2017; Yang et al., 2017). Advanced modes (PeakForce quantitative nanomechanical mapping (PF-QNM) and AFM-based infrared spectroscopy (AFM-IR)) allow for the simultaneous mapping of topography, mechanical stiffness and chemical composition (Eliyahu et al., 2015; Yang et al., 2017; Wagner et al., 2025). It provides a fingerprint for individual macerals through the utilization of photothermal expansion of the sample as a local infrared detector, allowing for the *in-situ* observation of molecular evolution and mechanical stiffening (Yang et al., 2017; Abarghani et al., 2020). AFM-IR also provides nanoscale evidence of chemical and microstructural heterogeneity on mirror-like surfaces of naturally deformed shales (Zhu et al., 2024). Newer variants, such as frequency-sweep force volume, enable measurements of mechanical damping (Q-factor). Compensation for mechanically induced resonance shifts improves the accuracy of the infrared response (Pittenger et al., 2019; Wagner et al., 2025).

Recent advances in AFM have enhanced the characterization of shale reservoirs, particularly in the quantitative analysis of pore structure, the characterization of organic matter evolution with thermal maturity, and the assessment of interfacial wettability. However, studies have largely focused on these individual technical dimensions, while the systematic integration of nanomechanics, geochemistry and fluid-solid interface behavior remains insufficient to reveal the multi-scale characteristics of shale reservoirs (Xiao et al., 2026). Specific pathways for translating AFM data into engineering applications have also been rarely discussed. CO_2-brine-shale interactions and mechanical responses under supercritical CO_2 ($ScCO_2$) conditions have been examined; however, a systematic review integrating multimodal AFM, PF-QNM, and AFM-IR data is still lacking. In this paper, the influence of the molecular evolution of organic matter during maturation on mechanical strength and anisotropic fracture toughness is evaluated. Through the integration of these nanoscale insights into multiscale rock physics modeling, a pathway is defined for upscaling microscopic properties to core-scale and seismic-scale predictions. Ultimately, this framework supports the identification of sweet spots for hydraulic fracturing and the assessment of carbon storage.

2. Foundational principles and advanced instrumentation of AFM in geoscience

The development of AFM in 1986 provided a critical cornerstone for nanotechnology through extending atomic-level imaging to nonconducting surfaces, overcoming the conductivity constraints of earlier scanning tunneling microscopy. For shale and reservoir systems, AFM can operate in gas or liquid environments without vacuum or conductive coatings. The core architecture consists of a flexible microfabricated cantilever, typically composed of Si or Si_3N_4, featuring an ultra-sharp tip. Typically, the tip radius is 2-20 nm and the cantilever spring constant ranges from 0.01 to 50 N/m (Ishida, 2024; Joo et al., 2025). As for shear-strength and adhesion analyses, specific protocols may involve pre-wearing the tip on a silicon substrate to obtain a stable geometry, that is typically greater than 50 nm. Cantilevers with bending constants of approximately 3.6 N/m have been used for consistent tribomechanical characterization (Tian et al., 2021; De Lacerda et al., 2023; Joo et al., 2025).

Scanning the heterogeneous rock surface in a line-by-line raster pattern creates a three-dimensional (3D) surface map (Fig. 1(a)). During scanning, cantilever displacements are tracked at the picometer scale. In beam-bouncing detection, a laser reflects from the rear of the cantilever onto a four-segment position-sensitive photodiode (Liu et al., 2022b; Ishida, 2024; Joo et al., 2025). This configuration also supports lateral force microscopy (Fig. 1(b)). Cantilever torsion caused by friction is registered in the lateral force channel. Topographic effects on friction images are reduced by subtracting

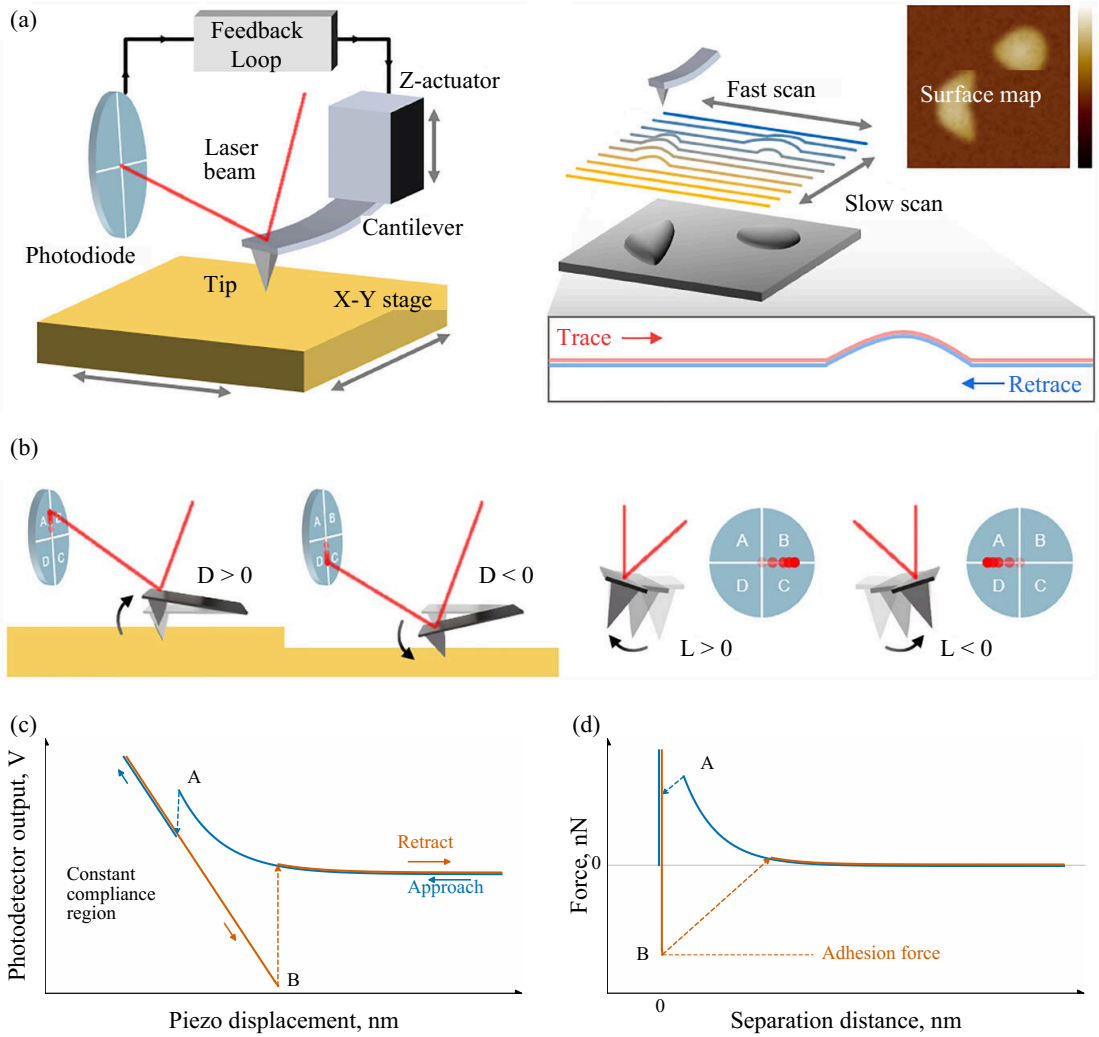

Fig. 1. Schematic configuration and force-spectroscopy principles of AFM: (a) System architecture and raster scanning (Joo et al., 2025), (b) vertical-deflection and lateral-twisting detection (Joo et al., 2025), (c) raw photodetector output and (d) force-separation curve for mechanical analysis.

backward-scan images from forward-scan images (Carpick et al., 1997; Karhu et al., 2009; De Lacerda et al., 2023). A closed-loop feedback system maintains a constant interaction force via adjusting the piezoelectric scanner. The lateral scan ranges are generally 30-100 μm, with vertical adjustments of approximately 10 μm. The contact mode is suitable for rigid mineral phases but can damage soft organic matter. The tapping mode oscillates the cantilever near its resonance frequency, reducing lateral forces and sample damage during kerogen or bitumen imaging. Functionalized probes coated with liquids, such as crude oil or fracturing fluid, can measure interaction forces directly at the solid-liquid interfaces (Ishida, 2024; Joo et al., 2025).

Beyond topographic visualization, AFM also provides quantitative nanomechanical characterization through force spectroscopy. A standard measurement cycle includes probe approach, contact and retraction to generate force-separation curves (Joo et al., 2025). The constant-compliance region is used to calculate the Young's modulus and hardness of individual shale components. The raw photodetector output and converted curve reveal critical mechanical phenomena (Figs. 1(c) and 1(d)). The jump-in effect at Point A occurs when attractive forces pull the cantilever toward the surface, while the jump-out effect at Point B quantifies the adhesion force required to separate the tip from the sample surface.

These capabilities are widened by advanced modes. For instance, Kelvin probe force microscopy (KPFM) maps contact potential differences to investigate surface-charge distributions and wettability (Ishida, 2024; Joo et al., 2025). Scanning Kelvin probe microscopy (SKPM) commonly uses a dual-channel procedure, where the first channel maps surface morphology through tapping mode, while the second measures surface potential at a fixed tip height (Ishida, 2024). These techniques have been used to characterize surface potential in shale reservoirs and charge variations in shale organic matter (Kang et al., 2025; Xu et al., 2025). AFM-IR integrates a pulsed tunable infrared laser with AFM to induce photothermal expansion. This approach can map chemical functional groups

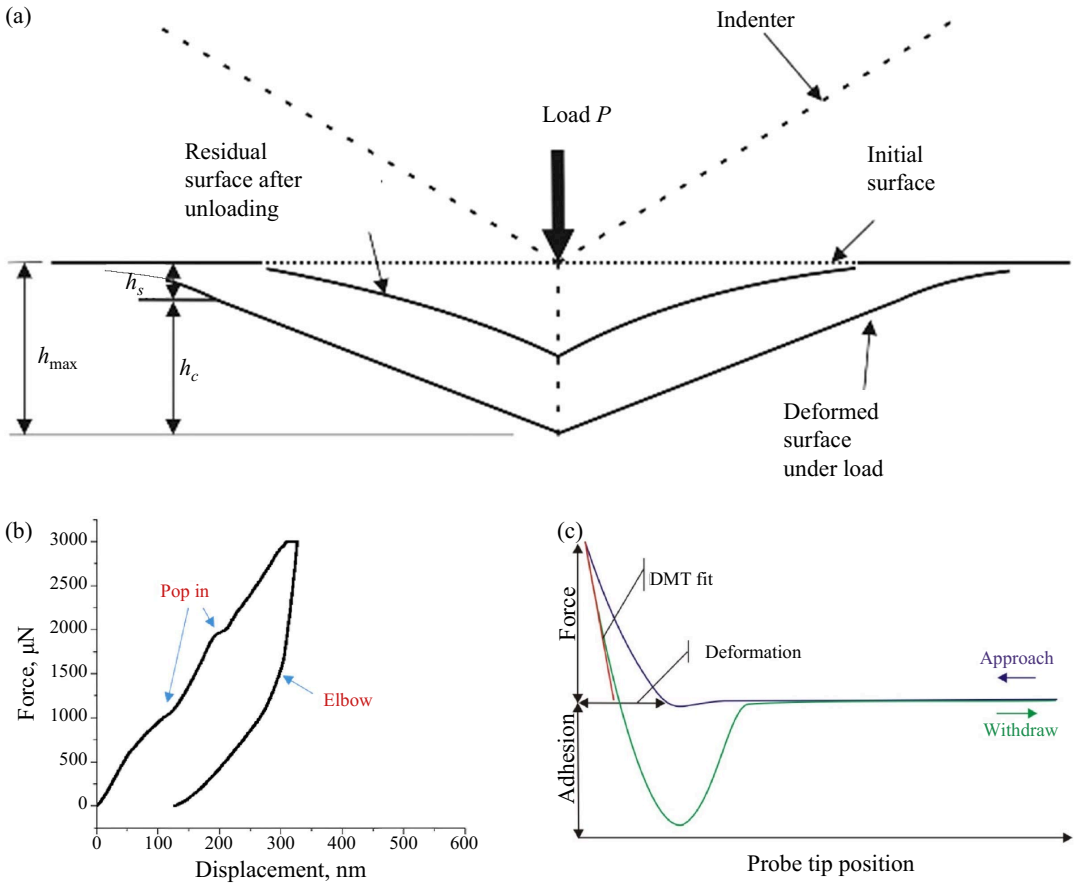

Fig. 2. Measurement geometries and force-response analysis for nanoindentation and AFM: (a) Schematic illustration of the unloading process (Liu et al., 2016), (b) nanoindentation load-displacement curve highlighting pore crushing and phase transitions and (c) AFM force-distance curve with DMT fitting and adhesion (Kong et al., 2021).

and molecular heterogeneity within the organic matrix. High-speed atomic force microscopy (HS-AFM) achieves imaging speeds of 1-20 frames per second through high-bandwidth feedback and high-resonance microcantilevers. It permits the real-time observation of dynamic processes such as fluid intrusion and microcrack propagation (Wang et al., 2021; Ishida, 2024; Joo et al., 2025).

3. Methodological frameworks and comparative analysis

To characterize organic-rich reservoirs and bridge the gap between nanoscale heterogeneity and macroscopic geomechanical response, a robust methodological framework is needed. Force spectroscopy techniques (primarily AFM and nanoindentation) are regarded as dual pillars of this characterization, although significant differences in the physical interaction with the sample surface have been observed (Kong et al., 2021; Wang et al., 2024). To address these complexities, recent protocols couple grid nanoindentation with scanning electron microscopy-energy-dispersive X-ray spectroscopy (SEM-EDS) to assign mechanical data to specific mineral phases at constituent scales of 5.8-11.7 μm (Mashhadian et al., 2018; Du et al., 2023). Nanoindentation typically uses a Berkovich diamond tip to apply milli-Newton loads. The resulting indentation depths are generally 250-350 nm or greater, and elastic modulus and hardness are determined by the Oliver-Pharr model (Kong et al., 2021; Wang et al., 2024). In organic-rich calcareous shales, high-load nanoindentation often yields a unimodal response of 40-50 GPa dominated by the mineral matrix. Meanwhile, lower loads are required to resolve softer organic matter with moduli of 5-10 GPa (Graham et al., 2021, 2023; Onwumelu et al., 2024). In comparison, AFM in PF-QNM or quantitative imaging (QI) modes applies ultra-low forces, typically 8-10 μN, producing indentation depths of 5-30 nm; it therefore probes individual particles rather than aggregates. These differences are reflected in the force-response curves (Figs. 2(b) and 2(c)). Nanoindentation curves may exhibit pop-in or elbow events associated with pore collapse or phase transformations. AFM force curves are fitted with Derjaguin-Muller-Toporov (DMT) or Hertz-Sneddon models to extract the reduced modulus while accounting for nanoscale adhesion (Graham et al., 2021; Kong et al., 2021; Wang et al., 2022b, 2024). AFM also provides high lateral resolution, commonly using 256 × 256 pixels over a 10 × 10 μm^2 area. In contrast, nanoindentation relies on the statistical deconvolution of grid datasets to distinguish organic matter, clay and mineral clusters (Kong et al., 2021).

Phase-identified nanoindentation combines Gaussian prob-

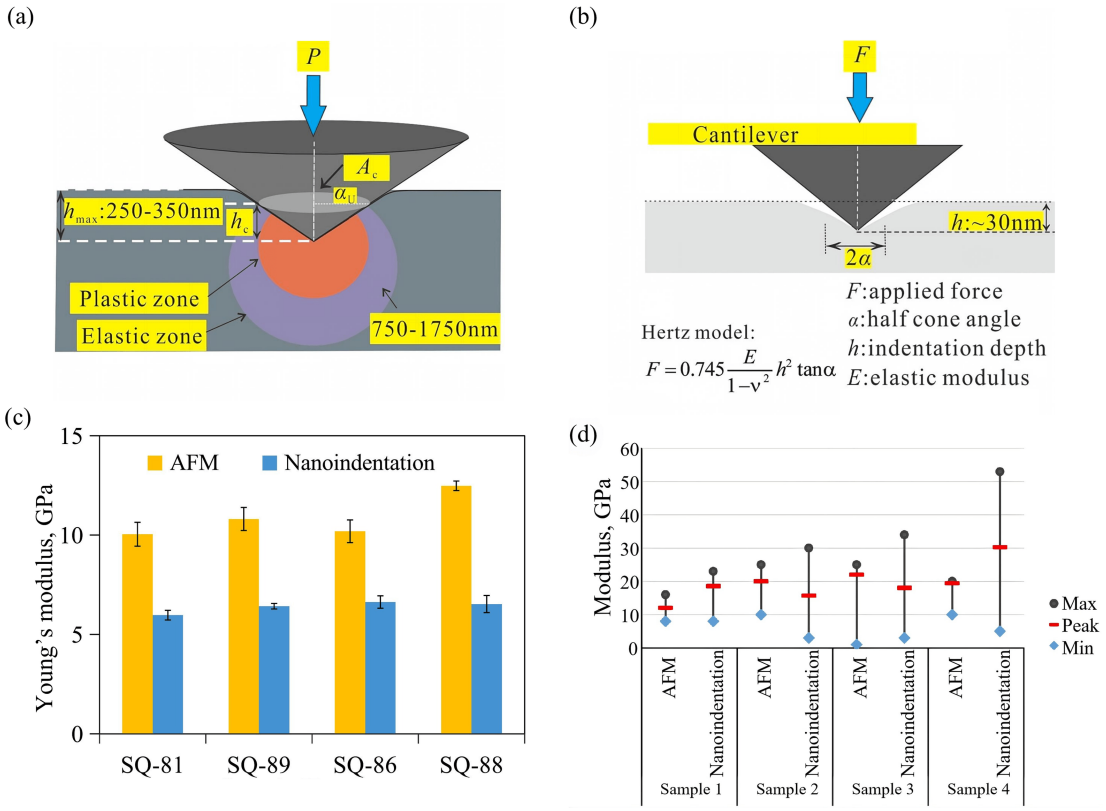

Fig. 3. Comparison of AFM and nanoindentation in organic-matter characterization: (a) AFM indentation zone, (b) nanoindentation deformation zone, (c) organic-matter Young's modulus measured by both methods (Wang et al., 2024) and (d) modulus distributions of the organic-matter/clay cluster (Kong et al., 2021).

ability density functions with physicochemical measurements to refine the mechanical properties of complex phases. This strategy addresses the limited mineralogical verification of conventional statistical deconvolution (Emmanuel et al., 2017; Du et al., 2023). However, significant discrepancies arise when nanoscale measurements are compared with bulk characterization. Water adsorption reduces indentation moduli in coal by 60%-66% because of swelling stress and mineral dissolution. In contrast, ultrasonic pulse-velocity tests may record a 17% increase in dynamic Young's modulus (Zhang et al., 2018a; Li et al., 2023b). Bulk methods measure an averaged dynamic response, whereas indentation and AFM resolve localized static degradation (Zhang et al., 2018a; Li et al., 2022). Fig. 3 illustrates the associated difference in the indentation and deformation zones. It can be seen that AFM probes an indentation zone of approximately 30 nm, while nanoindentation produces an elasto-plastic deformation zone of 750-1750 nm that may include mineral inclusions and micropores (Wang et al., 2024). Wang et al. (2024) observed that the nanoindentation moduli for organic matter were approximately twofold lower than AFM measurements, at 9.8 GPa versus 18.2 GPa (Figs. 3(a)-3(c)). Kong et al. (2021) reported complementary evidence from shales spanning a range of thermal maturities (Fig. 3(d)). Nanoindentation produces broad modulus distributions for organic matter-clay clusters, whereas AFM maintains phase-specific resolution within smaller domains. As a result, nanoindentation is useful for capturing grain-to-grain interactions, while AFM better resolves the intrinsic mechanical response of organic matter (Kong et al., 2021; Wang et al., 2024). Table 1 summarizes the comparative applicability of these techniques, providing a reference for method selection.

Even within a single method, modulus values reported for the same component by different laboratories can still differ considerably. For organic matter, Young's modulus ranges from approximately 4 GPa (Wang et al., 2022b) to as high as approximately 25 GPa (Eliyahu et al., 2015), whereas quartz values extend from 63 ± 8 GPa (Eliyahu et al., 2015) to 90-115 GPa (Gong et al., 2024). After accounting for depositional environment and thermal maturity, the remaining discrepancies often reflect methodological factors. PF-QNM and QI use different feedback and fitting protocols. The reported peak-force set points are from 500 nN to 8 μN (Fender et al., 2020; Kong et al., 2021; Wang et al., 2024), while tip radii span approximately 8-40 nm. Diamond probes offer superior wear resistance for wide modulus ranges, while Si/Si_3N_4 probes are typically preferred for organic-matter-dominated samples requiring higher imaging resolution (Charlton et al., 2021; Wang et al., 2022b). Under the DMT model, the apparent modulus correlates negatively with the square root of tip radius. The tip radius can increase substantially during continuous scanning, with reported changes from 14 to 21 nm and from 10 to 19 nm (Liu et al., 2018b; Zhang et al., 2022a). For highly adhesive soft organic matter, the choice between

Table 1. Comparative applicability of AFM and nanoindentation techniques in shale.

Method	Typical research objectives	Applicable conditions	Limitations
Nanoindentation (Berkovich; single-point and grid arrays)	Mineral-phase modulus and hardness; statistical partitioning of mechanical phases; upscaling to reservoir scale.	mN-scale loads; indentation depths $\geq$ 250-350 nm; grid arrays require Gaussian deconvolution.	Deformation zone may yield composite moduli; soft organic matter masked by mineral response.
Grid nanoindentation + SEM-EDS	Direct mineral-phase identification and mechanical characterization.	Constituent length scales of $\sim$5.8-11.7 μm; Gaussian deconvolution constrained by EDS composition.	Complex workflow; effective resolution limited to aggregate scale.
Hold-segment nanoindentation	Creep and viscoelastic behavior.	Instrument thermal stability; sufficient holding duration; drift correction.	Thermal drift; apparent negative creep artifacts.
AFM force spectroscopy (contact mode)	Modulus and hardness of individual constituents; adhesion force; LFM shear strength.	Tip pre-wear ($>$ 50 nm); calibrated cantilever constants.	Damage to soft organic matter; adhesion correction required; low acquisition efficiency.
AFM PF-QNM / QI	Intrinsic modulus and hardness of organic matter (across maturity); mechanical phase identification.	Flat, low-roughness polished surfaces; typical 8-10 μN, 5-30 nm shallow indentation.	Small scan areas with limited statistical representativeness; modulus sensitive to tip selection.
AFM contact / tapping-mode imaging	Surface morphology; 3D nanopore distribution; roughness; kerogen / solid bitumen imaging.	Contact mode for hard minerals; tapping mode for soft organic matter.	Damage to soft organic matter.
AFM functionalized / liquid-film probes	Solid-liquid interfacial forces; nanoscale wettability and adhesion.	Solid-liquid interfaces; tip coated with specific fluids; controlled fluid composition / salinity.	Adhesion measurements depend on probe geometry and coating stability.
AFM-KPFM / SKPM	Surface potential imaging (dry / water-wet / $ScCO_2$); indirect wettability assessment.	Gaseous or liquid-film environments; SKPM lift mode.	Tip lift reduces spatial resolution; absolute potential sensitive to ambient humidity and atmosphere.
AFM-IR	Nanoscale functional-group imaging; maturity-driven evolution; intra-particle heterogeneity.	Infrared-active functional groups only.	Near-surface sensitive; signal depends on tip-sample contact quality.
HS-AFM	Real-time observation of dynamic processes (fluid intrusion, micro-crack propagation).	High-bandwidth instrumentation; second-scale processes (1-20 frames/s).	Frame rate limits observable time scales.

Johnson-Kendall-Roberts and DMT models should be guided by the Tabor parameter. Assumed Poisson's ratios of 0.2-0.5 can introduce uncertainties of approximately 2%-25% (Li et al., 2018b; Zhang et al., 2022a; Wang et al., 2024). Mechanical polishing and argon-ion polishing produce roughness values of approximately 340 nm and 3 nm, respectively. Excess roughness can lead to modulus underestimation by increasing the estimated contact area (Bobji and Biswas, 1998). AFM cantilever spring constants can be obtained from thermal tuning, manufacturer specifications, or independent Sader-method and thermal-noise calibration (Hutter and Bechhoefer, 1993; Sader et al., 1999). For nanoindentation, load settings span more than two orders of magnitude, from 1 (Wang et al., 2024) to 500 mN (Charlton et al., 2021). Instrument calibration can follow the ISO 14577 series and established Oliver-Pharr correction procedures (Oliver and Pharr, 2004). Therefore, AFM and nanoindentation provide apparent quantities influenced by different deformation zones, as well as different model assumptions, and values obtained under different laboratory conditions should not be directly compared without normalization.

4. Nanoscale characterization of pore systems and surface topography

The application of AFM for heterogeneous porous media enables the high-resolution 3D visualization of nanopore spatial distribution and surface topography. This approach overcomes the resolution limits inherent to traditional SEM (Liu et al., 2019b; Zhao et al., 2019; Chen et al., 2021). The surface roughness parameters, including arithmetic mean roughness (R_a) and root-mean-square roughness (R_q), are critical indices for quantifying matrix complexity and surface irregularities (Liu et al., 2019b; Chen et al., 2021; Morga and Wrzalik, 2025). For broad-sense shale oil reservoirs, lithology significantly influences these parameters. Fine sandstone typically exhibits the highest roughness ($R_a \approx$ 16.48 nm), while mudstone ($R_a \approx$ 4.79 nm) and siltstone ($R_a \approx$ 3.96 nm) have comparatively smoother surfaces due to their finer grain sizes (Shen et al., 2021). A systematic contrast is

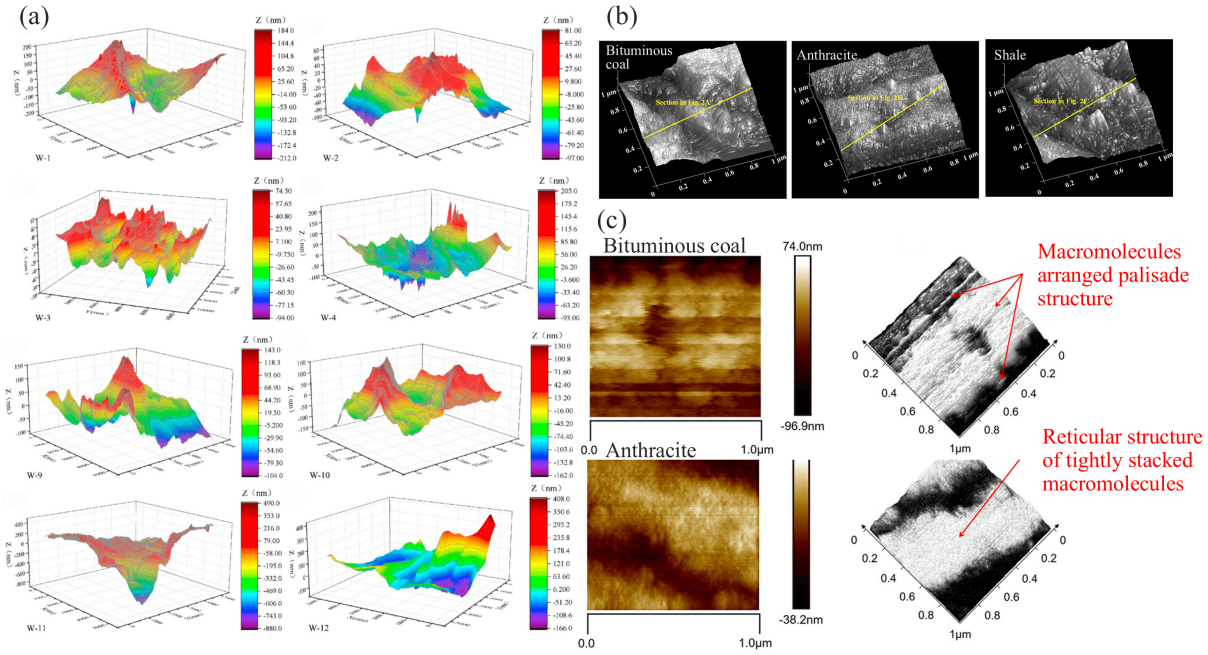

Fig. 4. 3D AFM surface morphology and roughness characteristics of shale and coal: (a) 3D morphology from organic-rich (W-1 to W-4) to organic-poor (W-11, W-12) samples (Chen et al., 2021), (b) 3D topographies of bituminous coal, anthracite and shale (Liu et al., 2019b) and (c) two-dimensional and 3D images of intermolecular pores in bituminous coal and anthracite (Wu et al., 2025).

observed across the organic-richness gradient of the Longmaxi Formation (Fig. 4(a)). Organic-rich shales possess smoother surfaces, with an average R_a of 38.74 nm and R_q of 49.91 nm. In comparison, organic-poor shales exhibit much higher R_a (104.58 nm) and R_q (138.80 nm) values, indicating rougher surfaces and greater topographic variation (Chen et al., 2021). In coal-bearing systems, surface roughness is also sensitive to thermal maturity. For example, as the surface becomes more regular and develops numerous smaller pores, R_a decreases from 18.04 nm in bituminous coal to 7.24 nm in anthracite (Liu et al., 2019b). Recent extensive datasets clarified that as vitrinite reflectance (R_o) increases from 1.43% to 3.15%, R_a declines linearly from approximately 31.45 to 5.86 nm. This negative correlation is driven by structural densification and aromatic condensation (Wu et al., 2025). The 3D topographies in Fig. 4(b) capture the two end-members of surface regularization, from the irregular high-relief bituminous coal to the smooth, regularly pored anthracite (Liu et al., 2019b). At the molecular scale, the loose grid-like arrangement of macromolecular clusters in bituminous coal contracts into a densely packed structure in anthracite (Fig. 4(c)). Accordingly, large wedge- and oval-shaped intermolecular pores shrink into smaller elliptical and circular ones. This coal sequence offers a mechanistic reference for surface regularization. Additionally, real shale roughness and pore characteristics are controlled by mineral frameworks, bedding, microfractures, and multiphase surfaces. Fast Fourier transform analysis of surface images can also discern heterogeneity, where mudstone surfaces appear more homogeneous (fewer bright spectral points) compared to the heterogeneous, anisotropic surfaces of siltstone and dolarenite (Shen et al., 2021).

The quantitative characterization of pore structural parameters through AFM involves pore number, areal porosity, and average pore diameter, with vertical resolutions down to 0.03 nm (Liu et al., 2019b; Chen et al., 2021). AFM also resolves micro-crack topography and vertical geometry, while DMT modulus mapping identifies low-stiffness zones around fractures (Fig. 5(a); Cheng et al., 2023). Two-dimensional height images, 3D topography, and section profiles further reveal surface undulations, with troughs indicating pores along selected sections (Fig. 5(b); Zhao et al., 2019). Through threshold segmentation and watershed analysis, the pore number, areal porosity and pore diameter distributions can be extracted from AFM images (Fig. 5(c)). The threshold method is suitable for pores of 10-500 nm, whereas watershed analysis is more appropriate for pores of 1-200 nm (Zhao et al., 2019). AFM-based pore characterization also provides morphological evidence for distinguishing primary biological pores from secondary pores formed during hydrocarbon generation (Guan et al., 2019; Morga and Wrzalik, 2025).

5. Mechanical response of organic macerals and inorganic minerals

Using high-resolution AFM mechanical mapping, four phases in the shale matrix can be identified. These comprise a stiff mineral phase (> 90 GPa), isolated grains (~ 60 GPa), an intergranular matrix (~ 30 GPa), and a soft organic phase (0-25 GPa) (Fan et al., 2021). Table 2 summarizes the principal mineral phases and their geological significance. PF-QNM is

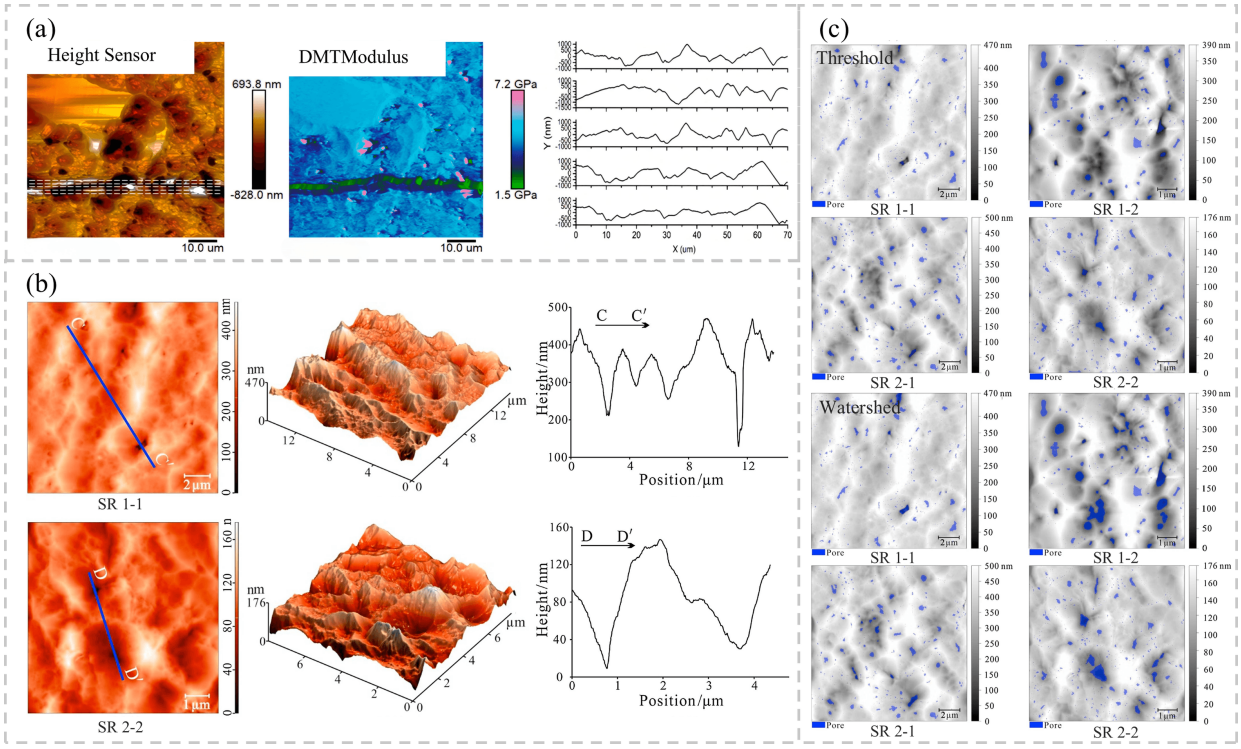

Fig. 5. AFM-based characterization of micro-cracks and quantitative analysis of nanopores in shale: (a) Height-sensor image, DMT modulus distribution, and sectional depth profiles of a micro-crack (Cheng et al., 2023), (b) two-dimensional height images, 3D topography, and section analysis of two shale samples (Zhao et al., 2019) and (c) pore identification by threshold segmentation and watershed analysis (Zhao et al., 2019).

Table 2. Mineral phases in shales and their geological significance (Eliyahu et al., 2015; Charlton et al., 2021; Fan et al., 2021; Gong et al., 2024).

Mineral type	Examples	Typical modulus range	Geological context	Role in shale behavior
Silicate framework	Quartz, feldspar, plagioclase	~60-115 GPa	Rigid skeletal grains	Controlling brittleness and fracture propagation
Carbonates	Calcite, dolomite	~70-120 GPa	Diagenetic cement in calcareous shales	Increasing stiffness with burial
Clay minerals	Illite, chlorite	~20-60 GPa	Intergranular matrix	Controlling viscoelastic deformation
Sulfides	Pyrite	>250 GPa locally	Framboidal inclusions	Creating strong heterogeneity
Organic-mineral matrix	Kerogen, clay, quartz	organic matter: ~0-25 GPa	Nanocomposite shale fabric	Governing deformation and storage
Diagenetic phases	Altered feldspar/carbonates	Variable	Burial alteration products	Modifying elasticity and reactivity

used to distinguish pyrite from quartz and calcite. Compact pyrite can have Young's moduli above 250 GPa, whereas the less compact framboidal pyrite typically falls within 120-160 GPa (Eliyahu et al., 2015; Gong et al., 2024). The reported bulk quartz moduli range from 77 to 96 GPa, but shale-surface measurements often average 63 ± 8 GPa because of crystallographic anisotropy and spatial averaging at the probe tip (Eliyahu et al., 2015). The intergranular clay matrix, mainly composed of illite and Fe-chlorite, consistently exhibits moduli of 29-35 GPa (Eliyahu et al., 2015). These ranges vary with crystallographic anisotropy, lattice defects, diagenetic recrystallization, and framboid development (Charlton et al., 2021; Gong et al., 2024).

As illustrated in Fig. 6(a), correlative backscattered-electron scanning electron microscopy (SEM-BSE) and AFM images can be used to identify organic matter within nanometer-scale voids between rigid mineral phases (Eliyahu et al., 2015). This compliant organic-rich framework strongly influences bulk rock deformation, and its importance is supported by the negative correlation between creep modulus and

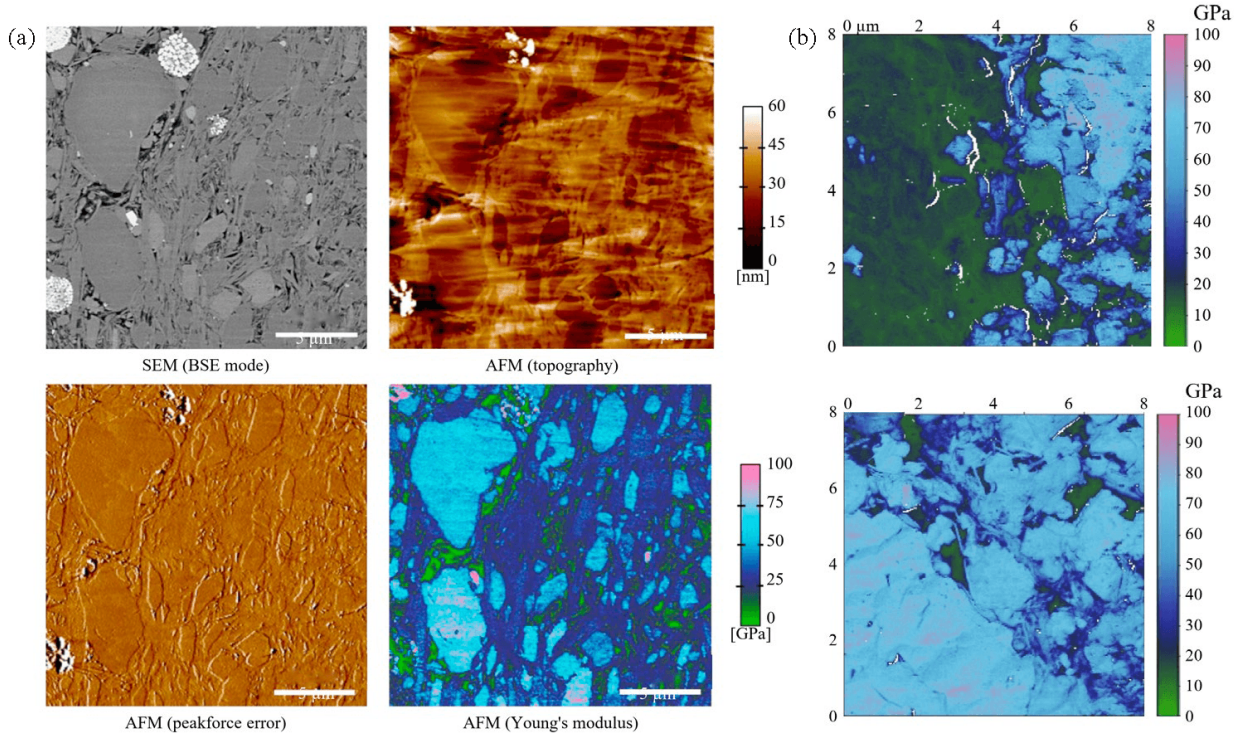

Fig. 6. AFM mechanical mapping from shale constituent identification to intra-particle organic-matter heterogeneity: (a) Correlative SEM-BSE, AFM topography, PeakForce error, and Young's modulus maps of the same field of view (Eliyahu et al., 2015) and (b) intra-particle modulus variations and localized boundary stiffening in organic matter (Li et al., 2018b).

total clay-kerogen content (Charlton et al., 2021).

The mechanical response of individual organic macerals depends on biogenic origin, initial kerogen type, and thermal maturity (Li et al., 2018a, 2018b). Disordered molecular structures and the physical mixing of macerals or kerogen-bitumen blends create additional heterogeneity within single particles (Jubb et al., 2020; Gong et al., 2024). Table 3 summarizes the structural evolution and nanomechanical characteristics of shale organic matter across different thermal maturity stages.

For Type I kerogen from the Green River oil shale, the *in-situ* Young's modulus is 5-11 GPa, reflecting the compliant nature of aliphatic-rich organic matter (Alstadt et al., 2016). Highly mature Type II/III organic matter exhibits a broader modulus distribution. Dry-gas-window samples have a modal Young's modulus of approximately 15-16 GPa and a secondary peak below 10 GPa, indicating persistent mechanical differentiation (Eliyahu et al., 2015). Molecular dynamics simulations yield the stiffness order Type III > Type II > Type I and show that confining pressure stiffens all three kerogen types (Wu and Firoozabadi, 2020). Therefore, kerogen type, thermal maturity and confining pressure jointly regulate organic-matter stiffness and strength through aliphatic content, aromatization and structural densification.

Solid bitumen and bituminite in the Bakken Formation are characterized by Young's moduli of 2.91-11.77 GPa, whereas that for bacterially derived granular micrinite reaches 23 GPa (Li et al., 2018a, 2018b). As shown in Fig. 6(b), high-resolution modulus maps also reveal pronounced intra-particle gradients and localized hardening at particle boundaries. In porous particles, a stiffer outer shell that is approximately 50-100 nm thick surrounds a softer inner core. This structure reflects both the internal organization of organic matter and its contact relationships with adjacent minerals (Eliyahu et al., 2015; Li et al., 2018b).

The viscoelastic nature of shale further complicates its nanomechanical response during indentation cycles. During the holding stage, displacement initially increases through creep and then decreases during unloading as elastic recovery dominates. After a critical holding time, storage modulus and hardness first decrease and then increase. Stiffer components with higher Young's moduli exhibit faster elastic recovery and more complex storage-modulus variations (Liu et al., 2019a; Zhang et al., 2022b; Liang et al., 2024). Diagenesis also modifies the mineral framework and causes the typical modulus ranges in Table 2 to differ among reservoirs (Charlton et al., 2021). Enhanced carbonate cementation at higher thermal maturities can increase the overall elastic response of the shale matrix (Abedi et al., 2016; Charlton et al., 2021). These mineral-organic interactions should therefore be considered when interpreting reservoir-scale mechanical behavior.

6. Geochemical evolution and maturity-dependent mechanical heterogeneity

The geochemical evolution of organic matter during thermal maturation is characterized by the systematic transformations of molecular functional groups. These transformations directly govern the nanoscale mechanical properties and het-

Table 3. Structural evolution and nanomechanical characteristics of shale organic matter across subsequent thermal maturity stages (Li et al., 2018a, 2018b; Jubb et al., 2020; Gong et al., 2024).

Kerogen category	Dominant precursors / Macerals	Thermal maturity stage	Structural evolution	Mechanical / Reservoir implication
Immature kerogen	Alginite, vitrinite, amorphinite	Early burial (R_o < ~0.7%)	Aliphatic-rich, oxygen-functional groups	Soft framework; low modulus
Oil-window kerogen	Transitional kerogen → bitumen	Moderate maturity (R_o ≈ 0.7%-1.0%)	Aromatization begins; hydrocarbon generation	Rapid stiffness increase
Gas-window kerogen	Pyrobitumen, condensed organic matter	High maturity (R_o > 1.3%)	Graphitic aromatic networks; nanopores	Gas storage and brittle behavior
Secondary organic matter	Solid bitumen infill	Post-generation	Void filling and pore development	Controls storage space
Carbonized organic matter	Highly condensed carbon	Late/overmature	Structural ordering and densification	Enhanced brittleness

erogeneity of organic matter (Wang et al., 2022a; Phan et al., 2023; Zhao et al., 2025). AFM-IR spectroscopy detects molecular vibrational modes at spatial resolutions of 10-20 nm. The key markers include aromatic C=C stretching (~1,600 cm^{-1}), aliphatic CH_2 bending (~1,450 cm^{-1}), and carbonyl/-carboxyl C=O stretching (~1,700-1,720 cm^{-1}) (Wang et al., 2022a; Phan et al., 2023; Zhao et al., 2025). As thermal maturity increases, the organic matrix becomes progressively enriched in aromatic functional groups, while oxygenated and aliphatic components are lost via decarboxylation and dealkylation (Zhang et al., 2022a; Phan et al., 2023). These transformations can be quantified by the A-factor (a proxy for H/C ratio) and the C-factor (a proxy for O/C ratio). Both indices decrease during catagenesis, reflecting the loss of aliphatic chains and oxygen-containing groups, along with enhanced aromaticity (Fig. 8(b)) (Wang et al., 2022a; Zhang et al., 2022a). With increasing maturity, long aliphatic chains and NSO compounds are progressively removed, leaving aromatic rings with short side chains (Fig. 8(a)) (Fender et al., 2020). In low-maturity shales, these chemical changes coincide with surface shrinkage, pore collapse and thermally induced cracking caused by labile-component degradation (Li et al., 2025).

High-resolution AFM-IR mapping reveals distinct chemical heterogeneity among organic particles (Fig. 7(a)). In the figure, each column represents one organic grain, with corresponding optical, topographic, CH_2, C=C, and C=O maps arranged by row. Some macerals, such as inertinite, show relatively uniform compositions dominated by aromatic C=C signals. In contrast, migrated solid bitumen and unclassified organic materials exhibit pronounced nanoscale variations. Single-point AFM-IR spectra of Longmaxi Shale samples further resolve the compositional differences among maceral types (Fig. 7(b)), where graptolite periderm has a predominantly aromatic signature. Pyrobitumen-clay composites are more porous than homogeneous pyrobitumen, consistent with their distinct chemical and structural properties (Zhao et al., 2025).

The nanomechanical response corresponding to these geochemical shifts can be described by an S-shaped evolutionary trend in the Young's modulus of organic matter with increasing R_o (Fig. 8(b)). Zhang et al. (2022a) established this relationship for vitrinite from organic-matter-rich mudstones in the Junggar Basin (R_o = 0.5%-1.5%) by combining PF-QNM modulus measurements with micro-Fourier transform infrared spectroscopy. At low maturity (R_o = 0.5%-0.7%), vitrinite is relatively soft with Young's modulus values of 3.04-3.19 GPa, and the broad frequency distribution indicates significant internal mechanical heterogeneity. Meanwhile, upon entering the main oil-generation stage (R_o ≈ 0.7%-1.0%), the Young's modulus of vitrinite increases sharply to 9.71 GPa. This pronounced hardening is consistent with the removal of long-chain aliphatic structures and oxygen-containing functional groups, together with enhanced aromatization. The rate of modulus increase gradually slows down at R_o = 1.0%-1.3%. At R_o = 1.3%-1.5%, the modulus rises only slightly to 13.29-13.94 GPa, while the probability distribution narrows, indicating reduced internal mechanical heterogeneity (Zhang et al., 2022a). The most significant stiffness increase occurs during the main oil-generation stage, coinciding with the transition from aliphatic-dominated to aromatic-dominated chemical frameworks. Therefore, this S-shaped relationship represents an empirical trend within a specific vitrinite series. Its applicability to other shale systems should be evaluated by considering kerogen type, organic maceral composition, depositional environment, and diagenetic history (Fender et al., 2020; Wu and Firoozabadi, 2020; Charlton et al., 2021; Gao et al., 2023).

AFM observations of different organic matter series further reveal diverse manifestations of the maturity-induced hardening process. For marine Type II kerogen, Emmanuel et al. (2016) similarly observed rapid hardening within the oil-generation window, followed by a relatively stable modulus up to R_o = 1.25%. Marine and lacustrine shales display distinct modulus distribution characteristics. For marine Type II kerogen, AFM measurements identify low- and high-modulus constituents whose proportions shift systematically with maturity (Fig. 8(c)). Low-modulus constituents fall at approximately 3-10 GPa, whereas high-modulus ones fall at approximately

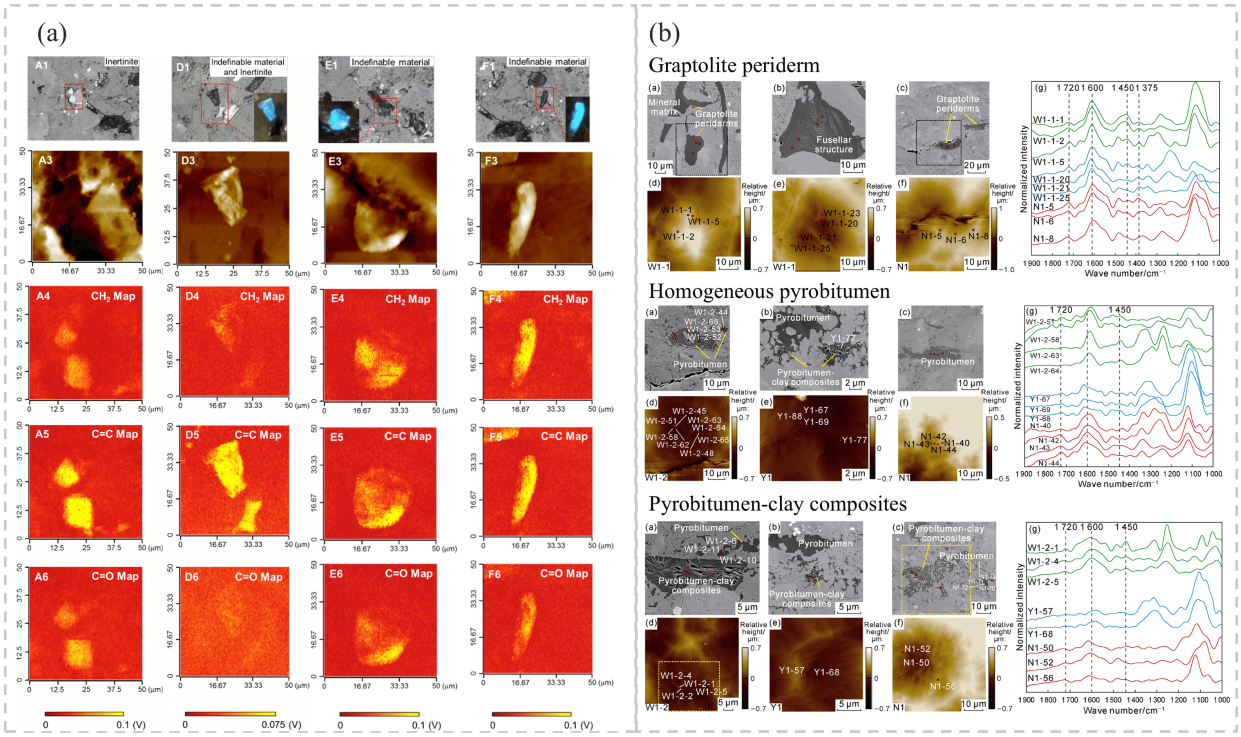

Fig. 7. Chemical characterization of organic matter in shale by AFM-IR: (a) Optical, topographic and functional-group maps of organic grains in the Bowland Shale (Wang et al., 2022a) and (b) SEM images, surface morphology, and single-point AFM-IR spectra of graptolite periderm, homogeneous pyrobitumen and pyrobitumen-clay composites in the Longmaxi Shale (Zhao et al., 2025).

19-24 GPa. Immature samples are dominated by low moduli. In the gas window, the high-modulus constituent accounts for 70%-80% (Fender et al., 2020). Lacustrine shales exhibit a different response pattern. Combined AFM and laser Raman measurements reveal distinct maceral responses in Type II kerogen shales from the Shahejie Formation, Bohai Bay Basin (Gao et al., 2023). As R_o increases from 0.78% to 1.10%, the macrinite modulus increases from 4.89 to 6.02 GPa. In contrast, the vitrinite modulus changes from 3.04 to 3.76 GPa and then decreases to 2.47 GPa, displaying a non-monotonic evolution. Lithology and diagenesis further modulate the mechanical evolution of organic matter. These lithological and diagenetic effects are demonstrated by the differences between carbonate-rich and silica-rich shales, together with the high composite moduli of overmature authigenic-carbonate-rich samples (Fender et al., 2020; Charlton et al., 2021).

7. Reservoir dynamics and fluid-solid interface characteristics

The interaction between reservoir fluids and the rock matrix is governed by nanoscale surface-potential heterogeneity, hydrated cation bridges, and wettability alteration (Kang et al., 2025; Tian et al., 2026). KPFM reveals strong spatial variations in the surface potential of shale, with typical values ranging from tens to hundreds of millivolts (Tian et al., 2022; Kang et al., 2025). These variations are closely related to polar oxygen-containing functional groups, including carboxyl (-COOH) and hydroxyl (-OH), on organic-matter surfaces (Kang et al., 2025). AFM colloidal-probe measurements show that kerogen exhibits stronger adhesion than adjacent inorganic minerals in both continental and marine shales. The measured adhesion forces are 100.86 ± 5 μN and 94.28 ± 4.7 μN, respectively (Tian et al., 2018). The large surface dipole moments of C=C and C=O bonds enhance interfacial adhesion and influence hydrocarbon adsorption at organic pore walls and organic-mineral interfaces. In addition, fluid exposure can further rearrange surface charges and alter adhesion.

The interaction between oil and rock is further stabilized by hydrated cation bridges in the formation brine. Metal cations (Na^+, Ca^{2+}, and Al^{3+}) connect polar oil components, such as stearic acid, to negatively charged surface groups through water molecules and hydrogen bonds. Ca^{2+} and Al^{3+} have stronger hydration capacities and larger hydrated radii than Na^+; therefore, they form more robust hydrogen-bonding networks and stronger interfacial adhesion. Molecular dynamics simulations and AFM measurements reveal that these bridges increase oil-film flow resistance, particularly under high-salinity conditions (Fig. 9) (Hu et al., 2021b). Reducing multivalent-cation concentrations can disrupt these bridges and promote oil-film detachment, providing a nanoscale explanation for low-salinity water flooding. However, these simulations and AFM measurements use silica as a simplified model interface, whereas real shale pore walls contain multiple minerals, organic functional groups, and complex pore geometries, which may alter bridge formation and strength.

The dynamics of the fluid-solid interface are also sensitive to surface topography and fluid chemistry. AFM experiments

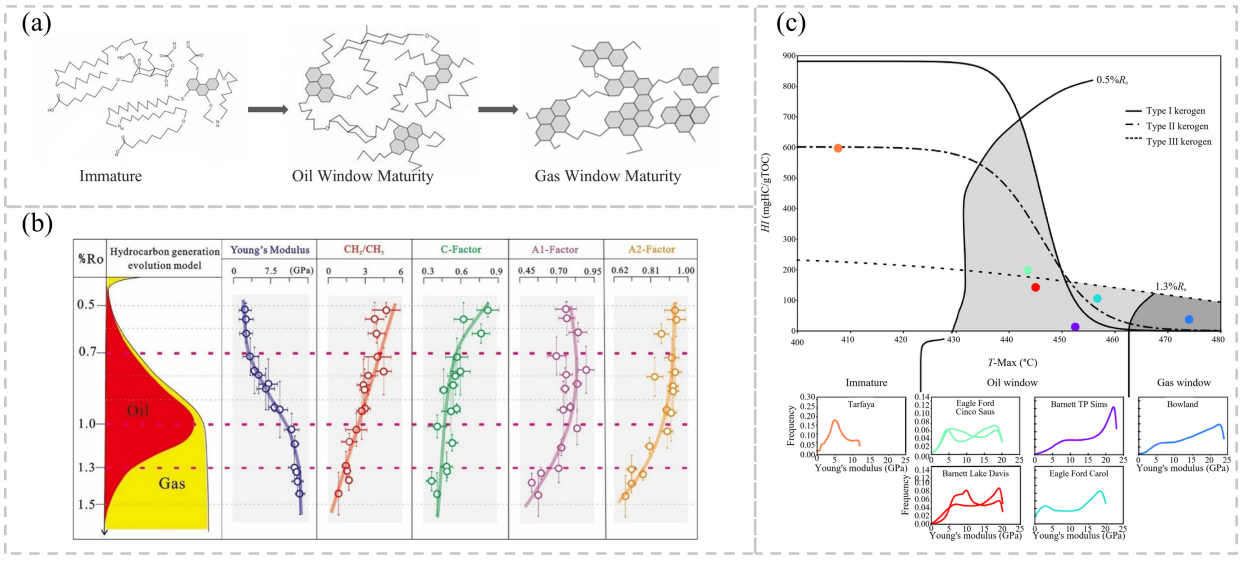

Fig. 8. Maturity-dependent chemical and mechanical evolution of organic matter: (a) Molecular structure evolution of kerogen (Fender et al., 2020), (b) staged S-shaped evolution of Young's modulus for vitrinite, coupled with hydrocarbon generation and molecular indices (Zhang et al., 2022a) and (c) T_{max}-HI plot and Young's modulus distributions of Type II kerogen (Fender et al., 2020).

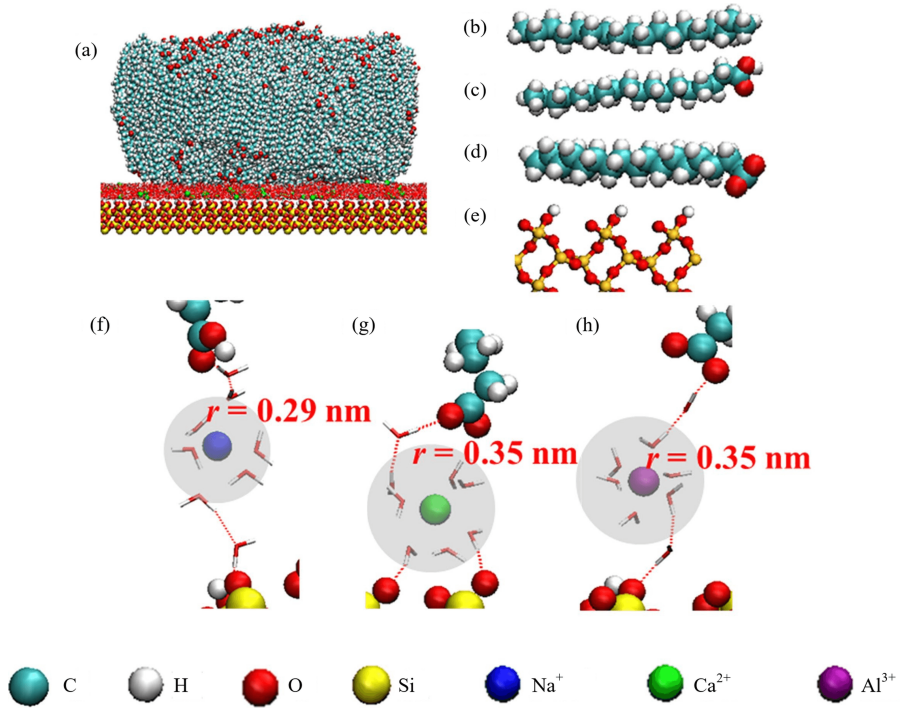

Fig. 9. Hydrated cation bridges at the oil-brine-silica interface: (a) Molecular model of the thin brine layer, (b)-(e) molecular components, including 18-alkane, stearic acid, stearate, and silica and (f)-(h) hydrated bridges formed by Na^+, Ca_2^+, and Al_3^+ (Hu et al., 2021b).

using oil-modified probes on mica revealed that adhesion increases with surface roughness because of enlarged contact areas. The measured forces reached 14-30 nN at separation distances of 5-10 nm and vanished beyond 40 nm (Bai et al., 2022). These mica experiments provide a simplified model for understanding the effect of surface roughness on adhesion at mineral surfaces. In shale samples, slickwater promotes clay swelling and dispersion, as well as carbonate dissolution, and these reactions increase surface roughness by up to 75.04% and reduce the DMT modulus (Dai et al., 2025). The dimensionless wetting index I further reduces roughness-related bias in adhesion-work measurements and improves comparisons of local adhesion properties (Huo et al., 2024).

The reliability of nanoscale reservoir characterization depends on how closely the test conditions match the *in-situ* environment. Most existing AFM data are acquired under ambient or dry conditions, whereas reservoir rocks experience elevated temperatures, pressures and complex pore fluids. Water-shale interaction can decrease the elastic modulus by 0.6%-15% and hardness by 8.6%-17.8% (Liu et al., 2021a). Sample drying history also affects pore characterization. Conventional air drying can underestimate pore volume by 19%-84% in clay-rich materials, while critical-point drying better preserves the native microstructure (De Kimpe, 1984; Suleimenova et al., 2014). Heating during kerogen isolation may also collapse nanopore networks. Notably, temperature fluctuations alone can induce microfractures in shale (Chen et al., 2025). Comparisons of hydrous and anhydrous pyrolysis further show that temperature-water coupling drives different mechanical evolution pathways for organic matter and minerals (Emmanuel et al., 2017; Sun et al., 2026). AFM colloidal probes can also quantify adhesion between kaolinite and different crude-oil fractions. These measurements combine approach-retract force curves with fraction-specific infrared spectroscopy to resolve differences in functional-group binding (Liu et al., 2021b). However, *in-situ* AFM measurements of shale matrices under oil-bearing conditions remain limited.

Variable-temperature AFM has enabled conducting *in-situ* measurements in mineral systems. A heating stage was used to quantify dissolution kinetics at 25-55 °C and extract an activation energy of 54 ± 4 kJ/mol (Kuwahara, 2008). Hydrothermal AFM has extended liquid-phase imaging to 150 °C and approximately 0.6 MPa (Higgins et al., 1998). Commercial heating stages can support PF-QNM or QI measurements at 250-300 °C, while thermal drift and cantilever calibration remain important limitations. Therefore, high-temperature shale studies often use heat treatment followed by room-temperature AFM measurements (Liang et al., 2024; Onwumelu et al., 2024). High-pressure fluid cells provide another approach, but they control pore-fluid pressure rather than confining pressure or axial stress. Their pressure limit is approximately 10 MPa, and most systems are custom-built (Lea et al., 2011). Stable quantitative PF-QNM mapping under these conditions remains challenging, particularly for studies of supercritical fluids that require the simultaneous control of temperature, pressure and fluid chemistry.

8. Applications of AFM in shale carbon capture, utilization and storage

Shale oil and gas reservoirs are increasingly recognized as promising targets for CO_2 geological utilization and sequestration (Merey and Sinayuc, 2016; Zhou et al., 2019). On the one hand, CO_2-shale interactions promote carbonate dissolution, clay alteration, and feldspar transformation, whereas quartz remains relatively stable under conventional reservoir conditions (Lu et al., 2019; Zhou et al., 2019). On the other hand, supercritical or near-critical CO_2 can extract light organic components, thereby modifying the pore structure and interfacial properties (Zhou et al., 2019; Wang et al., 2022b).

Wettability evolution influences capillary trapping, relative permeability and CO_2 injectivity. Macroscopic contact-angle measurements indicate that organic-matter shale can become completely CO_2-wet, with a contact angle of 180° in CO_2-brine systems at 30 MPa and 343 K. Under the same conditions, the contact angle against CH_4 is only 50°-90° (Pan et al., 2018). Molecular dynamics simulations attribute this transition to CO_2 film formation (Zhou et al., 2022). However, contact angles provide millimeter-scale averages and cannot resolve nanoscale wettability heterogeneity. AFM adhesion measurements can capture these local differences. Quantitative tests reveal adhesion forces of 56.5 ± 5 nN for quartz grains on shale surfaces, while this ranges from 30-44 nN for clay regions within the same field of view, indicating a wettability contrast greater than 40% (Mitiurev et al., 2021). KPFM further resolves the charge rearrangement associated with fluid exposure (Fig. 10(a)). Dry organic matter shows negative surface potentials ranging from -120.10 to -83.26 mV, mainly due to polar oxygen-containing functional groups. Water contact shifts the surface potential to approximately +240 mV and alters interfacial adhesion. A similar charge reversal occurs under water-$ScCO_2$ conditions, indicating that surface charge rearrangement contributes to wettability changes in CO_2-brine systems (Kang et al., 2025).

CO_2 exposure modifies the nanomechanical properties of individual shale constituents differentially, with the degree of mechanical degradation following the order of carbonate > clay > organic matter > quartz (Memon et al., 2024). Nanoindentation results demonstrate that $ScCO_2$ treatment decreases shale hardness by 29.5%-32%, Young's modulus by 11%, and fracture toughness by approximately 11.3%, with clay-rich domains weakening significantly more than quartz-rich domains (Shi et al., 2020). The aqueous phase serves as a key amplifier of mechanical damage. Compared to dry CO_2, water-bearing fluids induce a significantly stronger weakening of quartz, organic matter and composite phases (Liu et al., 2022a; Li et al., 2023a; Cheng et al., 2024). AFM measurements complement these ensemble-averaged indentation results by resolving single-phase responses that indentation cannot isolate. Nevertheless, single-phase characterization via PF-QNM also captures opposite trends for organic matter under specific reservoir conditions. Under reservoir temperature and pressure conditions, such imaging reveals that $ScCO_2$ exposure increases the elastic modulus of organic matter by approximately 124%, indicating pronounced hardening (Fig.

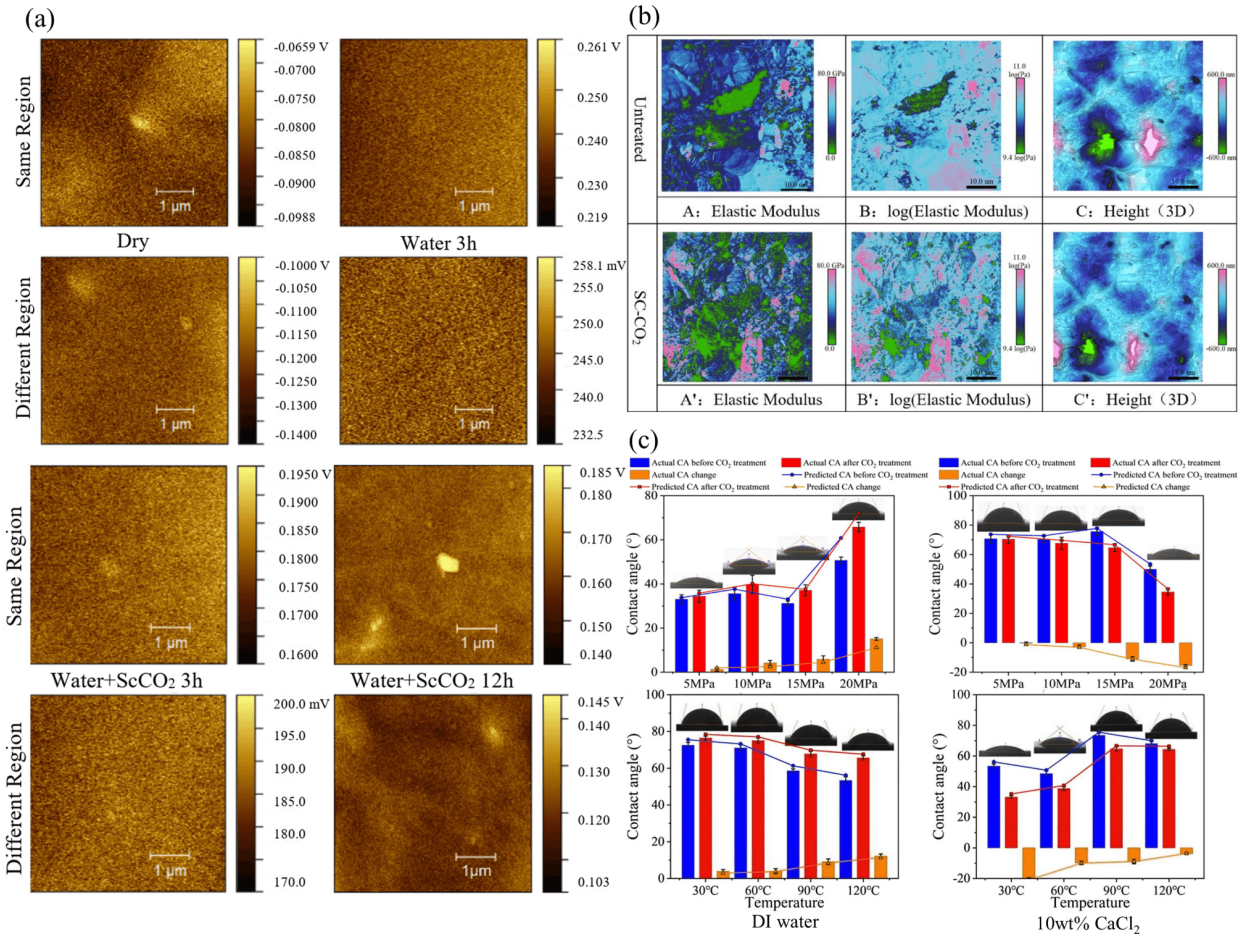

Fig. 10. Surface charge, mechanical and wettability responses of shale under CO_2-related fluid conditions: (a) Surface-potential evolution of organic matter under dry, water-wet and water-$ScCO_2$ conditions (Kang et al., 2025), (b) topography and elastic-property maps before and after $ScCO_2$ exposure (Wang et al., 2022b) and (c) water contact angles after CO_2 treatment at different pressures and temperatures in deionized water and 10 wt% $CaCl_2$ brine (Dai et al., 2024).

10(b)). This phenomenon arises from the solvent extraction of light and compliant components, increasing the relative proportion of the residual aromatic skeleton. Simultaneously, calcite develops higher porosity, rising from 7.1% to 8.1%, with a modulus decrease of approximately 6%, while both clay and organic matter undergo swelling (Wang et al., 2022b). The mineral weakening observed at the nanoscale is consistent with macroscopic reductions in an elastic modulus of 27%-48% after $ScCO_2$ treatment, with greater weakening in water-bearing systems (Meng et al., 2021). AFM characterization under reservoir temperature-pressure conditions links the contact-angle changes in Fig. 10(c) to CO_2-induced mineral reactions (Dai et al., 2024). Calcite dissolution in deionized water increases the water contact angle, indicating decreased caprock sealing integrity. In contrast, calcite precipitation in 10 wt% $CaCl_2$ brine decreases the contact angle. These results connect nanoscale mineral redistribution with wettability evolution.

Storage safety hangs on the balance among injection-zone weakening, adsorption-induced swelling, and caprock sealing integrity. During low-pressure CO_2 adsorption, the strain perpendicular to bedding can reach approximately 2.28 times that in the horizontal direction (Lin et al., 2025). Caprock experiments indicate that the breakthrough pressure of CO_2 is lower than that of CH_4/N_2, with an upper limit of approximately 6.2 MPa for mudstone. Sealing wettability also depends on mineral composition (Kim and Santamarina, 2013; Espinoza and Santamarina, 2017; Awad and Espinoza, 2024). These engineering responses involve CO_2 intercalation, competitive adsorption and swelling at the nanoscale interfaces (de Jong et al., 2014; Schaef et al., 2015; Zhang et al., 2018b). AFM can resolve the associated interfacial and mechanical changes and enable repeated measurements at the same location before and after $ScCO_2$ exposure. Combining these measurements with contact-angle, capillary-pressure and breakthrough-pressure experiments can support caprock sealing evaluation. Nevertheless, field-scale predictions require validation through core flooding, injection monitoring and history matching.

9. Future outlook: Artificial intelligence integration and multiscale modeling

The integration of artificial intelligence (AI) and deep learning provides valuable analytical capabilities for AFM-based characterization. These frameworks learn noise and structural features from large AFM image datasets to improve

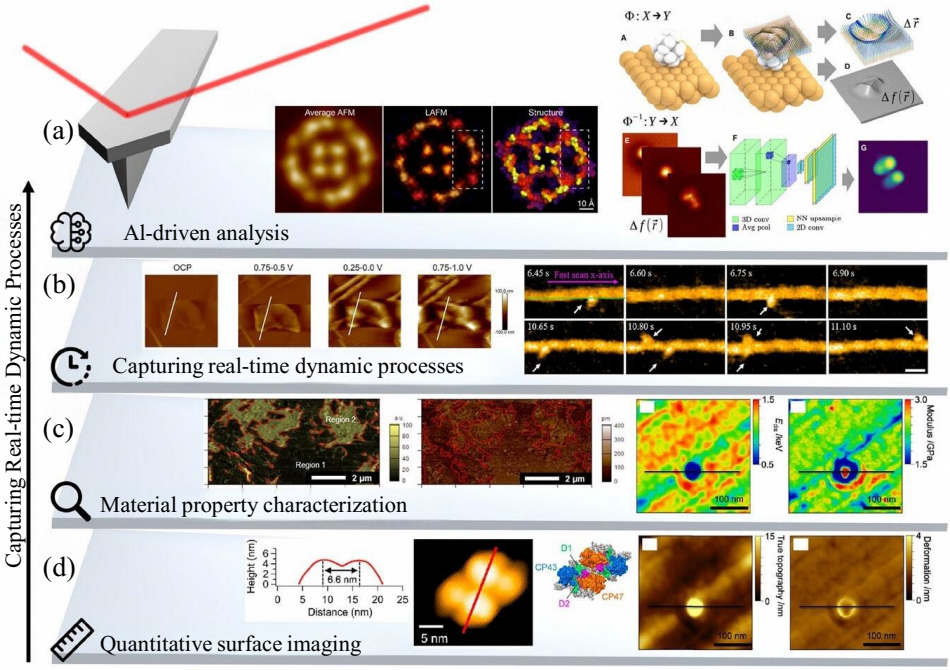

Fig. 11. Progressive integration of AFM characterization and AI-driven analysis: (a) AI-assisted molecular-structure prediction, (b) real-time process monitoring, (c) material-property mapping and (d) quantitative surface imaging (Joo et al., 2025).

the interpretation of complex surface structures. As illustrated in Fig. 11, progressing from quantitative surface imaging to AI-driven analysis can support automated 3D molecular-structure prediction and assist in identifying complex molecular configurations from AFM data (Zhang and Sun, 2021; Yang et al., 2023; Joo et al., 2025). AI-assisted sweet-spot evaluation and digital-twin development require validation against core, well-log and engineering-response data.

Simultaneously, the translation of nanoscale mechanical parameters into engineering-scale properties requires phase identification, homogenization and hierarchical validation. The modulus distributions of minerals and organic matter measured by AFM, once calibrated against SEM-EDS and X-ray diffraction, can serve as model inputs alongside the mechanical phase parameters obtained from statistical nanoindentation deconvolution. Suitable homogenization schemes include the Voigt-Reuss-Hill average, Mori-Tanaka, and self-consistent methods. These models must explicitly incorporate pores, micro-cracks and bedding anisotropy (Li et al., 2019; Charlton et al., 2021). However, the predictive accuracy of different homogenization schemes varies significantly. Numerical models based on mineral grains achieve errors within 5%, whereas Mori-Tanaka models using nanoindentation inputs exhibit deviations of 34%-133% for macroscopic moduli. The Voigt-Reuss-Hill average yields errors below 20% in most samples (Liu et al., 2025b; Wang et al., 2025). Upscaling accuracy therefore depends on both the homogenization scheme and the quality of mesoscale input data. Monte Carlo sampling can propagate uncertainties in phase properties to core-scale predictions. Currently, upscaling results are mostly validated at the core and single-well scales. At the same time, nanomechanical maps can serve as mesoscale inputs for digital twins and fracture propagation models (Zhang and Sun, 2021; Wu et al., 2026).

In engineering evaluation, upscaled modulus distributions can be combined with *in-situ* stress, fracture toughness, bedding, and natural fractures to constrain fracture propagation models. Microscale modulus can also be used to assess proppant embedment risk. When the shale modulus falls below approximately 6.89 GPa, embedment intensifies significantly, and elastic recovery accounts for less than 15% of the total embedment volume (Alramahi and Sundberg, 2012; Charlton et al., 2021). AFM-derived adhesion forces can constrain capillary-pressure and imbibition models after normalization by probe radius or calibration against adhesion work and contact angle (Huo et al., 2024; Yan et al., 2024). While these examples illustrate the engineering potential of AFM-derived parameters, field application requires further validation. Looking at a broader systems level, Fig. 12 complements these physics-based models by integrating resource efficiency, environmental impacts, and technological barriers into sustainability assessment (Liu et al., 2025a).

10. Conclusions

The characterization of shale reservoirs has been substantially advanced by AFM that bridges atomic-scale interactions with core-scale geomechanics. This review highlights that AFM provides superior spatial resolution for deciphering the intrinsic mechanical properties of individual organic macerals and nanopore networks, while grain-to-grain interactions are captured by traditional nanoindentation. The shale matrix comprises four distinct mechanical phases where organic matter (0-25 GPa) serves as the weakest link governing fracture propagation and wellbore stability. The structural reorganization of

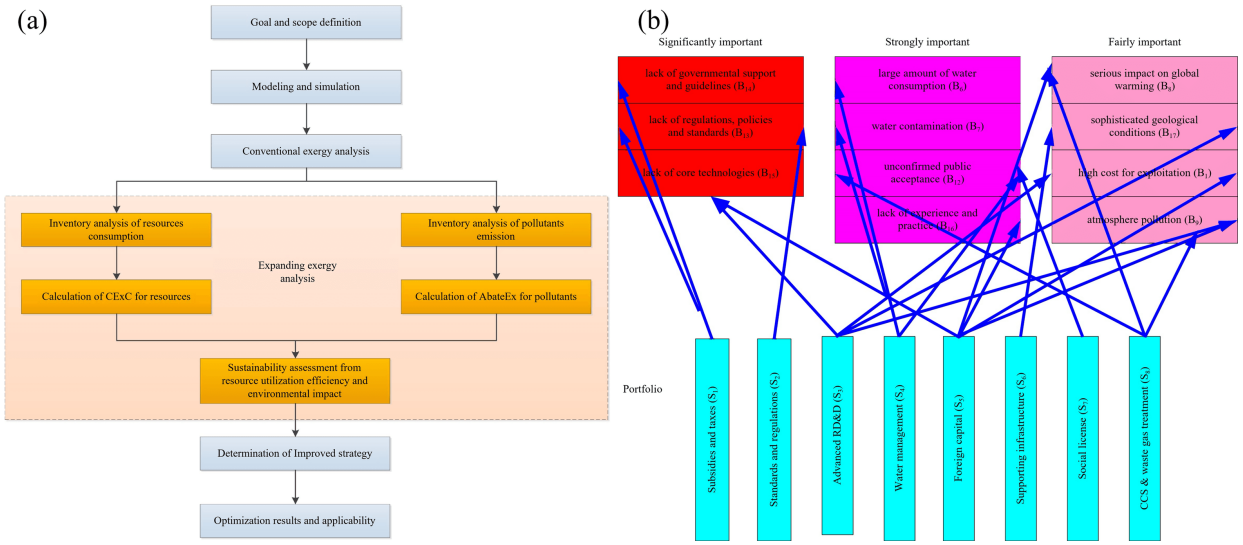

Fig. 12. Sustainability assessment and strategic planning for resource development: (a) Expanded-exergy assessment workflow and (b) barrier prioritization and strategy portfolio (Liu et al., 2025a).

kerogen, characterized by the loss of oxygenated groups and increased aromaticity, is induced by thermal maturation. This results in a sharp increase in mechanical stiffness at the oil-generation window (R_o approximately 0.7%-1.0%), followed by a plateau in the dry gas window. Nanoscale adhesion and wettability are heavily influenced by surface charge distributions. Oil film adhesion is significantly increased by the formation of hydrated cation bridges (particularly with Ca^{2+} and Al^{3+}), and this mechanism can be disrupted by low-salinity water flooding to enhance recovery. The future of reservoir characterization lies in the coupling of HS-AFM with deep learning algorithms, which could enable automated molecular structure prediction and the creation of digital twins. However, the identification of sweet spots and the assessment of carbon sequestration currently rest on laboratory-scale correlations, and their validation at the reservoir scale remains a significant research task.

Acknowledgments

The authors appreciate the support from the China National Petroleum Corporation-Peking University Strategic Cooperation Project of Fundamental Research, the National Science and Technology Major Project (No. 2026ZD1404502), and the National Natural Science Foundation of China (No. 42272150).

Conflicts of interest

The authors declare no competing interest.

Open Access This article is distributed under the terms and conditions of the Creative Commons Attribution (CC BY-NC-ND) license, which permits unrestricted use, distribution, and reproduction in any medium, provided the original work is properly cited.

References

Abarghani, A., Gentzis, T., Shokouhimehr, M., et al. Chemical heterogeneity of organic matter at nanoscale by AFM-based IR spectroscopy. Fuel, 2020, 261: 116454.

Abedi, S., Slim, M., Ulm, F.-J. Nanomechanics of organic-rich shales: The role of thermal maturity and organic matter content on texture. Acta Geotechnica, 2016, 11(4): 775-787.

Alramahi, B., Sundberg, M. I. Proppant embedment and conductivity of hydraulic fractures in shales. Paper ARMA-2012-291 Presented at 46th U.S. Rock Mechanics/Geomechanics Symposium, Chicago, Illinois, USA, 24-27 June, 2012.

Alstadt, K. N., Katti, K. S., Katti, D. R. Nanoscale morphology of kerogen and *in situ* nanomechanical properties of Green River oil shale. Journal of Nanomechanics and Micromechanics, 2016, 6(1): 04015003.

Awad, M. M., Espinoza, D. N. Mudrock wettability at pressure and temperature conditions for CO_2 geological storage. International Journal of Greenhouse Gas Control, 2024, 135: 104160.

Bai, T., Yang, F., Wang, H., et al. Adhesion forces of shale oil droplet on mica surface with different roughness: An experimental investigation using atomic force microscopy. Energies, 2022, 15(17): 6460.

Bennett, K. C., Berla, L. A., Nix, W. D., et al. Instrumented nanoindentation and 3D mechanistic modeling of a shale at multiple scales. Acta Geotechnica, 2015, 10(1): 1-14.

Bentley, R. W. Global oil & gas depletion: An overview. Energy Policy, 2002, 30(3): 189-205.

Bernard, S., Wirth, R., Schreiber, A., et al. Formation of nanoporous pyrobitumen residues during maturation of the Barnett Shale (Fort Worth Basin). International Journal of Coal Geology, 2012, 103: 3-11.

Bobji, M. S., Biswas, S. K. Estimation of hardness by nanoindentation of rough surfaces. Journal of Materials Research, 1998, 13(11): 3227-3233.

Bobko, C., Ulm, F.-J. The nano-mechanical morphology of shale. Mechanics of Materials, 2008, 40(4-5): 318-337.

Carpick, R. W., Ogletree, D. F., Salmeron, M. Lateral stiffness:

A new nanomechanical measurement for the determination of shear strengths with friction force microscopy. Applied Physics Letters, 1997, 70(12): 1548-1550.

Charlton, T. S., Goodarzi, M., Rouainia, M., et al. Effect of diagenesis on geomechanical properties of organic-rich calcareous shale: A multiscale investigation. Journal of Geophysical Research: Solid Earth, 2021, 126(7): e2020JB021365.

Chen, S., Li, X., Chen, S., et al. A new application of atomic force microscopy in the characterization of pore structure and pore contribution in shale gas reservoirs. Journal of Natural Gas Science and Engineering, 2021, 88: 103802.

Chen, Q., Tang, X., Shi, Y., et al. Nanomechanics and pore structure evolution in organic-rich shale reservoirs during high-temperature treatment: A multi-scale analysis of microscopic stability. Advances in Geo-Energy Research, 2025, 17(3): 241-255.

Cheng, S., Sheng, M., Xu, P. Application of AFM on identifying mechanical properties of individual minerals and surface properties of crack with high resolution in shale. Processes, 2023, 11(8): 2498.

Cheng, Q., Tang, J., Jia, Y., et al. Shale softening induced by CO_2 injection in the absence and presence of water: An experimental investigation based on nanoindentation. Energy, 2024, 288: 129653.

Curiale, J. A. Origin of solid bitumens, with emphasis on biological marker results. Organic Geochemistry, 1986, 10(1-3): 559-580.

Dai, J., Raza, A., Wang, T., et al. Impact of CO_2-brine-shale interaction on wettability change at reservoir temperature and pressure via AFM characterization. Energy & Fuels, 2024, 38(21): 21042-21051.

Dai, Q., Sun, W., Zuo, Y., et al. Impact of slickwater fracturing fluid on pore structure and micromechanical properties of clay-rich shale using fluid intrusion and AFM experiments. ACS Omega, 2025, 10(6): 6164-6181.

Dazzi, A., Prater, C. B. AFM-IR: Technology and applications in nanoscale infrared spectroscopy and chemical imaging. Chemical Reviews, 2017, 117(7): 5146-5173.

de Jong, S. M., Spiers, C. J., Busch, A. Development of swelling strain in smectite clays through exposure to carbon dioxide. International Journal of Greenhouse Gas Control, 2014, 24: 149-161.

De Kimpe, C. R. Effect of air-drying and critical point drying on the porosity of clay soils. Canadian Geotechnical Journal, 1984, 21(1): 181-185.

De Lacerda, D. L. P., Prioli, R., Parizek-Silva, Y. M., et al. Nanoscale identification and characterization of the shear strength of minerals and organic matter in shale. Frontiers in Earth Science, 2023, 11: 1132118.

Du, J., Whittle, A. J., Hu, L., et al. Coupling grid nanoindentation and surface chemical analysis to infer the mechanical properties of shale mineral phases. Engineering Geology, 2023, 325: 107304.

Eliyahu, M., Emmanuel, S., Day-Stirrat, R. J., et al. Mechanical properties of organic matter in shales mapped at the nanometer scale. Marine and Petroleum Geology, 2015, 59: 294-304.

Emmanuel, S., Eliyahu, M., Day-Stirrat, R. J., et al. Impact of thermal maturation on nano-scale elastic properties of organic matter in shales. Marine and Petroleum Geology, 2016, 70: 175-184.

Emmanuel, S., Eliyahu, M., Day-Stirrat, R. J., et al. Softening of organic matter in shales at reservoir temperatures. Petroleum Geoscience, 2017, 23(2): 262-269.

Espinoza, D. N., Santamarina, J. C. CO_2 breakthrough–Caprock sealing efficiency and integrity for carbon geological storage. International Journal of Greenhouse Gas Control, 2017, 66: 218-229.

Fan, M., Han, Y., Tan, X., et al. Experimental and numerical characterization of lower Huron Shale as a heterogeneous material. Rock Mechanics and Rock Engineering, 2021, 54(8): 4183-4200.

Fender, T. D., Van Der Land, C., Rouainia, M., et al. The assessment of organic matter Young's modulus distribution with depositional environment and maturity. Journal of Geophysical Research: Solid Earth, 2020, 125(12): e2020JB020435.

Gao, Y., Liu, B., Fu, X., et al. Nanomechanical and chemical variations of inertinite and vitrinite within lacustrine shale during oil generation. Marine and Petroleum Geology, 2023, 154: 106318.

Gong, Z., Chen, S., Ishimwe, H., et al. Study on microscale mechanical properties of minerals and organic matter in shale based on atomic force microscopy. AAPG Bulletin, 2024, 108(3): 495-520.

Graham, S. P., Rouainia, M., Aplin, A. C., et al. Geomechanical characterisation of organic-rich calcareous shale using AFM and nanoindentation. Rock Mechanics and Rock Engineering, 2021, 54(1): 303-320.

Graham, S. P., Aplin, A. C., Rouainia, M., et al. A micromechanical investigation of diagenetically-induced changes to the anisotropic elastic properties of calcareous mudstones. Geomechanics and Geophysics for Geo-Energy and Geo-Resources, 2023, 9(1): 107.

Guan, Q., Lü, X., Dong, D., et al. Origin and significance of organic-matter pores in upper ordovician wufeng-lower silurian longmaxi mudstones, sichuan basin. Journal of Petroleum Science and Engineering, 2019, 176: 554-561.

Han, L., Shi, X., Ni, H., et al. Review of CO_2 fracturing and carbon storage in shale reservoirs. Energy & Fuels, 2024, 38(17): 15913-15934.

Higgins, S. R., Eggleston, C. M., Knauss, K. G. A hydrothermal atomic force microscope for imaging in aqueous solution up to 150 °C. Review of Scientific Instruments, 1998, 69(8): 2994-2998.

Hu, T., Pang, X., Jiang, F., et al. Movable oil content evaluation of lacustrine organic-rich shales: Methods and a novel quantitative evaluation model. Earth-Science Reviews, 2021a, 214: 103545.

Hu, Y., Chu, Z., Dai, C., et al. Probing of the hydrated cation bridges in the oil/brine/silica system via atomic force microscopy and molecular dynamics simulation. Fuel, 2021b, 306: 121666.

Huo, X., Sun, L., Chen, F., et al. Quantitative characterization of adhesion work on shale surfaces and discussion on the

influence of roughness based on atomic force microscopy (AFM). ACS Omega, 2024, 9(28): 30859-30872.

Hutter, J. L., Bechhoefer, J. Calibration of atomic-force microscope tips. Review of Scientific Instruments, 1993, 64(7): 1868-1873.

Hutton, A., Bharati, S., Robl, T. Chemical and petrographic classification of kerogen/macerals. Energy & Fuels, 1994, 8(6): 1478-1488.

Ishida, N. Atomic force microscopy, in Non-Destructive Material Characterization Methods, edited by A. Otsuki, S. Jose, M. Mohan and S. Thomas, Elsevier, Amsterdam, pp. 89-125, 2024.

Javadpour, F., Moravvej Farshi, M., Amrein, M. Atomic-force microscopy: A new tool for gas-shale characterization. Journal of Canadian Petroleum Technology, 2012, 51(4): 236-243.

Joo, S., Eom, S., Choi, Y., et al. Atomic force microscopy for cross-disciplinary materials research. Small Methods, 2025, 9(11): 2500514.

Jubb, A. M., Birdwell, J. E., Hackley, P. C., et al. Nanoscale molecular composition of solid bitumen from the Eagle Ford Group across a natural thermal maturity gradient. Energy & Fuels, 2020, 34(7): 8167-8177.

Kang, Y., Ning, Z., Lyu, F., et al. Evolution of surface adhesion property and surface charge of shale organic matter at the nanoscale: Quantitative measurements by AFM and KPFM. Applied Surface Science, 2025, 695: 162919.

Karhu, E., Gooyers, M., Hutter, J. L. Quantitative friction-force measurements by longitudinal atomic force microscope imaging. Langmuir, 2009, 25(11): 6203-6213.

Khatibi, S., Ostadhassan, M., Tuschel, D., et al. Raman spectroscopy to study thermal maturity and elastic modulus of kerogen. International Journal of Coal Geology, 2018, 185: 103-118.

Kim, S., Santamarina, J. C. CO_2 breakthrough and leak-sealing - Experiments on shale and cement. International Journal of Greenhouse Gas Control, 2013, 19: 471-477.

Kong, L., Hadavimoghaddam, F., Li, C., et al. AFM vs. Nanoindentation: Nanomechanical properties of organic-rich shale. Marine and Petroleum Geology, 2021, 132: 105229.

Kuwahara, Y. In situ observations of muscovite dissolution under alkaline conditions at 25-50 °C by AFM with an air/fluid heater system. American Mineralogist, 2008, 93(7): 1028-1033.

Lea, A. S., Higgins, S. R., Knauss, K. G. A high-pressure atomic force microscope for imaging in supercritical carbon dioxide. Review of Scientific Instruments, 2011, 82(4): 043709.

Li, C., Ostadhassan, M., Gentzis, T., et al. Nanomechanical characterization of organic matter in the Bakken formation by microscopy-based method. Marine and Petroleum Geology, 2018a, 96: 128-138.

Li, C., Ostadhassan, M., Guo, S., et al. Application of PeakForce tapping mode of atomic force microscope to characterize nanomechanical properties of organic matter of the Bakken Shale. Fuel, 2018b, 233: 894-910.

Li, C., Ostadhassan, M., Kong, L., et al. Multi-scale assessment of mechanical properties of organic-rich shales: A coupled nanoindentation, deconvolution analysis, and homogenization method. Journal of Petroleum Science and Engineering, 2019, 174: 80-91.

Li, Y., Chen, J., Elsworth, D., et al. Nanoscale mechanical property variations concerning mineral composition and contact of marine shale. Geoscience Frontiers, 2022, 13(4): 101405.

Li, N., Jin, Z., Zhang, S., et al. Micro-mechanical properties of shale due to water/supercritical carbon dioxide-rock interaction. Petroleum Exploration and Development, 2023b, 50(4): 1001-1012.

Li, Z., Li, G., Li, H., et al. Effects of shale swelling on shale mechanics during shale-liquid interaction. Energy, 2023a, 279: 128098.

Li, Y., Wu, T., Zhao, J., et al. Thermal evolution of organic matter in low-maturity shale: A multimodal nanoscale investigation. Energy & Fuels, 2025, 39(16): 7739-7750.

Liang, Z., Jiang, Z., Tang, X., et al. Mechanical properties of shale during pyrolysis: Atomic force microscopy and nano-indentation study. International Journal of Rock Mechanics and Mining Sciences, 2024, 183: 105929.

Lin, S., Chang, X., Wang, K., et al. Swelling damage characteristics induced by CO_2 adsorption in shale: Experimental and modeling approaches. Journal of Rock Mechanics and Geotechnical Engineering, 2025, 17(9): 5526-5541.

Liu, K., Ostadhassan, M. Microstructural and geomechanical analysis of Bakken shale at nanoscale. Journal of Petroleum Science and Engineering, 2017, 153: 133-144.

Liu, K., Ostadhassan, M., Bubach, B. Applications of nanoindentation methods to estimate nanoscale mechanical properties of shale reservoir rocks. Journal of Natural Gas Science and Engineering, 2016, 35: 1310-1319.

Liu, K., Ostadhassan, M., Bubach, B. Application of nanoindentation to characterize creep behavior of oil shales. Journal of Petroleum Science and Engineering, 2018a, 167: 729-736.

Liu, K., Ostadhassan, M., Xu, X., et al. Abnormal behavior during nanoindentation holding stage: Characterization and explanation. Journal of Petroleum Science and Engineering, 2019a, 173: 733-747.

Liu, K., Qi, H., Wang, Z., et al. The organic matrix: An in-depth review of kerogen and its significance. Fuel, 2025a, 397: 135493.

Liu, X., Nie, B., Wang, W., et al. The use of AFM in quantitative analysis of pore characteristics in coal and coal-bearing shale. Marine and Petroleum Geology, 2019b, 105: 331-337.

Liu, Y., Liu, Q., Feng, G., et al. Upscaling mechanical properties of shale obtained by nanoindentation to macroscale using accurate grain-based modeling (AGBM). Energy, 2025b, 314: 134126.

Liu, Y., Liu, S., Kang, Y., et al. Probing nanomechanical properties of a shale with nanoindentation: Heterogeneity and the effect of water-shale interactions. Energy & Fuels, 2021a, 35(15): 11930-11946.

Liu, Y., Zou, G., She, J., et al. Nanoscale physical parameters of source rocks identified by atomic force microscopy: A

review. Geological Journal, 2022a, 57(10): 4345-4356.

Liu, Y., Xiong, Y., Li, Y., et al. Effect of thermal maturation on chemical structure and nanomechanical properties of solid bitumen. Marine and Petroleum Geology, 2018b, 92: 780-793.

Liu, Y., Zhang, S., Zou, C., et al. Quantitative measurement of interaction strength between kaolinite and different oil fractions via atomic force microscopy: Implications for clay-controlled oil mobility. Marine and Petroleum Geology, 2021b, 133: 105296.

Liu, Y., Liu, S., Liu, A., et al. Determination of mechanical property evolutions of shales by nanoindentation and high-pressure CO_2 and water treatments: A nano-to-micron scale experimental study. Rock Mechanics and Rock Engineering, 2022b, 55(12): 7629-7655.

Lu, Y., Chen, X., Tang, J., et al. Relationship between pore structure and mechanical properties of shale on supercritical carbon dioxide saturation. Energy, 2019, 172: 270-285.

Mashhadian, M., Verde, A., Sharma, P., et al. Assessing mechanical properties of organic matter in shales: Results from coupled nanoindentation/SEM-EDX and micromechanical modeling. Journal of Petroleum Science and Engineering, 2018, 165: 313-324.

Mastalerz, M., Schimmelmann, A., Lis, G. P., et al. Influence of maceral composition on geochemical characteristics of immature shale kerogen: Insight from density fraction analysis. International Journal of Coal Geology, 2012, 103: 60-69.

Mastalerz, M., Drobniak, A., Stankiewicz, A. B. Origin, properties, and implications of solid bitumen in source-rock reservoirs: A review. International Journal of Coal Geology, 2018, 195: 14-36.

Memon, S., Verrall, M., Lebedev, M., et al. Nanoscale analysis of shale matrix alteration after supercritical CO_2 treatment: Implications for $scCO_2$ fracturing in shales. Energy & Fuels, 2024, 38(3): 1873-1890.

Meng, S., Jin, X., Tao, J., et al. Evolution characteristics of mechanical properties under supercritical carbon dioxide treatment in shale reservoirs. ACS Omega, 2021, 6(4): 2813-2823.

Merey, S., Sinayuc, C. Analysis of carbon dioxide sequestration in shale gas reservoirs by using experimental adsorption data and adsorption models. Journal of Natural Gas Science and Engineering, 2016, 36: 1087-1105.

Mitiurev, N., Verrall, M., Shilobreeva, S., et al. Shale adhesion force measurements via atomic force microscopy. Oil & Gas Science and Technology - Revue d'IFP Energies nouvelles, 2021, 76: 73.

Morga, R., Wrzalik, R. Nanoporosity of graptolite periderm by atomic force microscopy (AFM): A case study from the Baltic Basin, Poland. International Journal of Coal Geology, 2025, 307: 104816.

Oliver, W. C., Pharr, G. M. Measurement of hardness and elastic modulus by instrumented indentation: Advances in understanding and refinements to methodology. Journal of Materials Research, 2004, 19(1): 3-20.

Onwumelu, C., Kolawole, O., Nordeng, S., et al. Analyzing thermal maturity effect on shale organic matter via PeakForce quantitative nanomechanical mapping. Rock Mechanics Bulletin, 2024, 3(3): 100128.

Pan, B., Li, Q., Wang, X., et al. CO_2 and CH4 wettabilities of organic-rich shale. Energy & Fuels, 2018, 32: 899-907.

Phan, V. T. H., Rebois, R., Beck, P., et al. Chemical functional characterization of immature and mature coals at the nanoscale by atomic force microscopy-based infrared spectroscopy (AFM-IR). International Journal of Coal Geology, 2023, 267: 104196.

Pittenger, B., Osechinskiy, S., Yablon, D., et al. Nanoscale DMA with the atomic force microscope: A new method for measuring viscoelastic properties of nanostructured polymer materials. JOM, 2019, 71(10): 3390-3398.

Sader, J. E., Chon, J. W. M., Mulvaney, P. Calibration of rectangular atomic force microscope cantilevers. Review of Scientific Instruments, 1999, 70(10): 3967-3969.

Schaef, H. T., Loring, J. S., Glezakou, V.-A., et al. Competitive sorption of CO_2 and H_2O in 2:1 layer phyllosilicates. Geochimica et Cosmochimica Acta, 2015, 161: 248-257.

Shen, R., Xiong, W., Lang, X., et al. Quantitative analysis of nano-scale pore structures of broad sense shale oil reservoirs using atomic force microscopy. Energy Exploration & Exploitation, 2021, 39(6): 1839-1856.

Shi, X., Jiang, S., Wang, Z., et al. Application of nanoindentation technology for characterizing the mechanical properties of shale before and after supercritical CO_2 fluid treatment. Journal of CO_2 Utilization, 2020, 37: 158-172.

Suleimenova, A., Bake, K. D., Ozkan, A., et al. Acid demineralization with critical point drying: A method for kerogen isolation that preserves microstructure. Fuel, 2014, 135: 492-497.

Sun, M., Fu, J., Ji, Y., et al. Contrasting mechanical evolution of Bakken shale under hydrous and anhydrous pyrolysis: A nanoindentation-based assessment. International Journal of Rock Mechanics and Mining Sciences, 2026, 203: 106526.

Tian, S., Dong, X., Wang, T., et al. Surface properties of organic kerogen in continental and marine shale. Langmuir, 2018, 34(46): 13882-13887.

Tian, X., Song, D., He, X., et al. Presenting *in situ* AFM investigations for the evolution of micro-surface topography and elastic modulus of rock under variable loads. Engineering Fracture Mechanics, 2021, 258: 108107.

Tian, X., He, X., Song, D., et al. AFM characterization of surface mechanical and electrical properties of some common rocks. International Journal of Mining Science and Technology, 2022, 32(2): 435-445.

Tian, H., Wang, X., Wang, X., et al. Wettability of shale/oil/brine and shale/oil/CO_2-enriched brine systems: Insights for CO_2 huff-and-puff enhanced shale oil recovery and geological storage. Advances in Colloid and Interface Science, 2026, 348: 103730.

Tyson, R. V. Palynological kerogen classification, in Sedimentary Organic Matter: Organic Facies and Palynofacies, edited by R. V. Tyson, Chapman & Hall, London, pp. 341-365, 1995.

Ulm, F.-J., Abousleiman, Y. The nanogranular nature of shale. Acta Geotechnica, 2006, 1(2): 77-88.

Wagner, M., Hu, Q., Hu, S., et al. Force volume atomic force microscopy-infrared for simultaneous nanoscale chemical and mechanical spectromicroscopy. ACS Nano, 2025, 19(19): 18791-18803.

Wang, K., Taylor, K. G., Ma, L. Advancing the application of atomic force microscopy (AFM) to the characterization and quantification of geological material properties. International Journal of Coal Geology, 2021, 247: 103852.

Wang, K., Ma, L., Taylor, K. G. Nanoscale geochemical heterogeneity of organic matter in thermally-mature shales: An AFM-IR study. Fuel, 2022a, 310: 122278.

Wang, T., Wang, Q., Zhang, P., et al. Application of atom force microscope and nanoindentation to characterize nanoscale mechanical properties of shale before and after supercritical CO_2 immersion. Journal of Petroleum Science and Engineering, 2022b, 212: 110348.

Wang, J., Dziadkowiec, J., Liu, Y., et al. Combining atomic force microscopy and nanoindentation helps characterizing *in situ* mechanical properties of organic matter in shale. International Journal of Coal Geology, 2024, 281: 104406.

Wang, J., Yang, C., Guo, Y., et al. Examining the reliability of current micro- and nano-indentation-based rock mechanical upscaling schemes: A comprehensive comparison with uniaxial/triaxial macroscopic mechanical testing. Geomechanics and Geophysics for Geo-Energy and Geo-Resources, 2025, 11(1): 28.

Wu, T., Firoozabadi, A. Mechanical properties and failure envelope of kerogen matrix by molecular dynamics simulations. The Journal of Physical Chemistry C, 2020, 124(4): 2289-2294.

Wu, D., Wei, J., Zhao, S., et al. Automatic identification and quantification of surface nanoscale pore morphology in coals of different ranks based on AFM, SEM and LP-N2GA. Journal of Microscopy, 2025, 300(3): 366-383.

Wu, Y., Liu, Z., Liu, Y., et al. Surrogate model for fracture propagation in heterogeneous reservoirs based on generative neural networks. Geoenergy Science and Engineering, 2026, 257: 214169.

Xiao, L. -Z., Jin, Y., Zhang, L. -B., et al. One hundred grand challenges in petroleum science. Petroleum Science, 2026, 23(8): 4477-4487.

Xu, Y., Lun, Z., Pan, Z., et al. Occurrence space and state of shale oil: A review. Journal of Petroleum Science and Engineering, 2022, 211: 110183.

Xu, L., Shen, R., Yang, H., et al. Utilizing atomic force microscopy for microstructural surface analysis and reservoir evaluation of shale. Arabian Journal for Science and Engineering, 2025, 50(7): 5253-5263.

Yan, X., Dai, C., Wang, R., et al. Experimental study on countercurrent imbibition in tight oil reservoirs using nuclear magnetic resonance and AFM: Influence of liquid-liquid/solid interface characteristics. Fuel, 2024, 358: 130026.

Yang, J., Hatcherian, J., Hackley, P. C., et al. Nanoscale geochemical and geomechanical characterization of organic matter in shale. Nature Communications, 2017, 8(1): 2179.

Yang, Y., Liu, F., Zhang, Q., et al. Recent advances in multiscale digital rock reconstruction, flow simulation, and experiments during shale gas production. Energy & Fuels, 2023, 37(4): 2475-2497.

Zeszotarski, J. C., Chromik, R. R., Vinci, R. P., et al. Imaging and mechanical property measurements of kerogen via nanoindentation. Geochimica et Cosmochimica Acta, 2004, 68(20): 4113-4119.

Zhang, Y., Lebedev, M., Al-Yaseri, A., et al. Nanoscale rock mechanical property changes in heterogeneous coal after water adsorption. Fuel, 2018a, 218: 23-32.

Zhang, M., de Jong, S. M., Spiers, C. J. Swelling stress development in confined smectite clays through exposure to CO_2. International Journal of Greenhouse Gas Control, 2018b, 74: 49-61.

Zhang, T., Sun, S. An exploratory multi-scale framework to reservoir digital twin. Advances in Geo-Energy Research, 2021, 5(3): 239-251.

Zhang, R., Cao, J., Hu, W., et al. Nanomechanical characterization of organic-matter maturity by atomic force microscopy (AFM). International Journal of Coal Geology, 2022a, 261: 104094.

Zhang, W., Zhang, D., Zhao, J. Experimental study of the influence of geochemical features on the viscoelasticity of organic matter in shale. Marine and Petroleum Geology, 2022b, 143: 105785.

Zhao, J., Liu, K., Zhao, S., et al. Response of organic matter pore development to functional groups in overmature marine shale: Insights from AFM-IR spectroscopy. Petroleum Exploration and Development, 2025, 52(2): 445-458.

Zhao, S., Li, Y., Wang, Y., et al. Quantitative study on coal and shale pore structure and surface roughness based on atomic force microscopy and image processing. Fuel, 2019, 244: 78-90.

Zhou, J., Hu, N., Xian, X., et al. Supercritical CO_2 fracking for enhanced shale gas recovery and CO_2 sequestration: Results, status and future challenges. Advances in Geo-Energy Research, 2019, 3(2): 207-224.

Zhou, J., Zhang, J., Yang, J., et al. Mechanisms for kerogen wettability transition from water-wet to CO_2-wet: Implications for CO_2 sequestration. Chemical Engineering Journal, 2022, 428: 132020.

Zhu, H., Lu, Y., Pan, Y., et al. Nanoscale mineralogy and organic structure characterization of shales: Insights via AFM-IR spectroscopy. Advances in Geo-Energy Research, 2024, 13(3): 231-236.

Zhu, H., Ju, Y., Lu, Y., et al. Natural evidence of organic nanostructure transformation of shale during bedding-parallel slip. GSA Bulletin, 2025, 137(5-6): 2719-2746.

Zou, C., Zhu, R., Chen, Z. -Q., et al. Organic-matter-rich shales of China. Earth-Science Reviews, 2019, 189: 51-78.